CANCER

Matrix stress relaxation drives glioblastoma cell response in viscoelastic biomaterials

Sadegh Ghorbani[1,2], Michelle S. Huang[3], Daiyao Zhang[3], Yueming Liu[1], Christopher Long[1], Riley Zwetsloot[1], Esther A.T. Mozipo[4], Rameshwar R. Rao[5,6], Annika Enejder[1], Sarah C. Heilshorn[1]*

The extracellular matrix (ECM) of glioblastoma (GBM) is known to modulate cell behavior, yet the specific contributions of matrix biochemical and biomechanical signaling remain poorly understood. To address this, we engineer a tunable hyaluronan-elastin-like protein (HELP) hydrogel to independently control ligand presentation and matrix viscoelasticity. Two peptides mimicking fibronectin (FBN) and tenascin-C (TNC) are incorporated into HELP along with hyaluronan, all of which are highly up-regulated in GBM. Using dynamic covalent chemistry, we develop hydrogels with matched stiffness but distinct stress relaxation profiles. Slow stress-relaxing matrices promote cell clustering and elevated expression of P-selectin, a GBM invasion marker. These matrices also result in increased nascent ECM production, increased lipid droplet storage, and altered cytokine secretion. Our results highlight the benefit of protein-engineered, viscoelastic biomaterials for modeling the tumor microenvironment and reveal matrix viscoelasticity as a critical regulator of GBM cell state, offering a tool for identifying previously unrecognized therapeutic targets.

INTRODUCTION

Glioblastoma (GBM) is recognized as the most aggressive and prevalent brain cancer in adults (*1*, *2*). The tumor microenvironment plays a critical role in GBM cell survival and invasion, and in particular, the biochemical and biomechanical properties of the extracellular matrix (ECM) have been suggested to contribute to the treatment-resistant nature of GBM (*3*). Although several studies have implicated matrix stiffness in altering GBM invasiveness (*4*, *5*), most of these three-dimensional (3D) in vitro GBM models have focused on purely elastic materials, which do not recapitulate the time-dependent mechanical behavior of native brain tissue. In vivo, both healthy brain and GBM tissues exhibit pronounced viscoelasticity, undergoing time-dependent deformation and stress relaxation upon applied strain (*6*, *7*). Moreover, GBM tissues display altered viscoelastic behavior compared to adjacent nontumor tissue, with faster stress relaxation dynamics observed in tumor regions (*8*).

More broadly, viscoelasticity is becoming increasingly recognized as a critical property of the cellular microenvironment that strongly affects cellular phenotype (*7*, *9*). In vivo, the microenvironment represents a complex system of biomechanical and biochemical cues, where the matrix stress relaxation rate, stiffness, and biochemical ligands are all changing simultaneously (*10*, *11*). Thus, there is a critical need for engineered tissue models that enable a reductionist approach to deconvolute these multiple, cellular inputs (*12*). Recent in vitro studies have begun to address this gap by designing engineered viscoelastic microenvironments, demonstrating that matrix viscoelasticity, independent of stiffness, serves as a critical biophysical cue regulating key features of GBM progression, including cell proliferation, gene expression, migration, and response to chemotherapy (*13*–*15*). For instance, stress-relaxing hydrogels have been reported to enhance GBM invasive morphology and chemoresistance (*15*). These findings emphasize the importance of incorporating viscoelastic properties into engineered models of the GBM microenvironment to more accurately identify mechanobiological contributions to tumor behavior.

In vivo, changes in GBM matrix viscoelasticity coincide with biochemical changes in matrix composition. Analyses of patient-derived GBM specimens have revealed elevated levels of ECM proteins, including fibronectin (FBN) and tenascin-C (TNC), as well as glycosaminoglycans like hyaluronic acid (HA), compared with healthy brain (*16*–*18*). In particular, TNC expression is enriched in the tumor core compared to the invasive margins, and such spatial differences correlate with variation in ECM mechanics (*19*, *20*). These findings emphasize the need for in vitro GBM models that can mimic both the biochemical complexity and the biomechanical diversity of the tumor microenvironment.

To address this, we engineered a 3D viscoelastic hydrogel system based on HA and engineered proteins incorporating bioactive peptide sequences derived from FBN and TNC. Engineering viscoelastic biomaterials with tunable stress relaxation properties can be achieved through several material design approaches, including interpenetrating polymer networks or hydrogels with reversible cross-links such as weak physical associations or dynamic covalent chemistry bonds (*14*, *17*–*19*). Here, we use dynamic covalent chemistry as a reversible cross-linking mechanism, with hydrogel stability further enhanced through the incorporation of self-associating elastin-like sequences (*21*). Our hydrogel design allows for independent tuning of matrix viscoelasticity, specifically, stress relaxation kinetics, while maintaining constant peptide presentation and stiffness, enabling us to investigate the distinct contributions of both viscoelasticity and ECM protein ligand presence on GBM cell behavior.

We demonstrate that GBM cell lines remain viable and proliferative within these hydrogels. By tuning the stress relaxation kinetics of the hydrogels while maintaining consistent peptide presentation and matrix stiffness, we observed distinct shifts in GBM cell behavior and

[1]Department of Materials Science and Engineering, Stanford University, Stanford, CA 94305, USA. [2]Department of Health Technology, Technical University of Denmark, 2800 Kgs. Lyngby, Denmark. [3]Department of Chemical Engineering, Stanford University, Stanford, CA 94305, USA. [4]Department of Bioengineering, Stanford University, Stanford, CA 94305, USA. [5]Ben Towne Center for Childhood Cancer and Blood Disorders Research, Seattle Children's Research Institute, Seattle, WA 98101, USA. [6]Division of Pediatric Hematology, Oncology, Bone Marrow Transplant, and Cellular Therapies, Department of Pediatrics, University of Washington School of Medicine, Seattle, WA 98105, USA.
*Corresponding author. Email: heilshorn@stanford.edu

phenotype. Notably, slower stress-relaxing matrices promoted cell clustering and increased expression of P-selectin, a cell adhesion molecule implicated in GBM invasion and immune modulation (*22*, *23*). In contrast, faster stress-relaxing matrices enhanced cell spreading and down-regulated P-selectin expression. Moreover, higher nascent ECM production and lipid droplet (LD) accumulation were found under the slow-relaxing condition, further supporting a shift in cell state driven by matrix viscosity. These results indicate that the dissipative properties of the matrix act as a potent regulator of GBM cell morphology, phenotype, and ECM remodeling. Ultimately, our findings highlight the utility of protein-engineered, viscoelastic biomaterials as platforms to investigate how dynamic mechanical cues in a defined tumor microenvironment with relevant biochemical cues influence GBM cell state.

RESULTS

Matrix stress relaxation plays a key role in modulating GBM cell morphology and P-selectin expression

To investigate how matrix viscoelasticity modulates GBM cell phenotype and behavior, we formulated a family of recombinant protein-based hydrogels that enable independent tuning of stress relaxation without altering matrix stiffness or ligand presentation. This previously reported hydrogel strategy, composed of HA and elastin-like proteins (ELPs), form a dynamic 3D platform termed HELP, providing programmable mechanical and biochemical environments for cell encapsulation across different applications (*21*, *24*, *25*). To customize the biochemical cues for relevance to the GBM microenvironment, we genetically engineered the recombinant ELP backbone to contain peptide motifs derived from FBN (RGD) and TNC (PLAEIDGIELTY). The TNC-derived peptide PLAEIDGIELTY was selected as a defined integrin-binding motif known to target the α9β1 integrin (*26*, *27*). This peptide originates from the FBN type III domain of TNC, enabling modular incorporation into the ELP backbone while preserving independent control over matrix mechanics and ligand presentation. The α9β1 integrin has been implicated in GBM migratory behavior (*21*, *28*, *29*). Both proteins are known to be highly expressed in GBM tissues, particularly in perivascular and tumor core regions (*30*–*33*), where they regulate cell adhesion and invasion.

The HA and ELP polymers were each used at 1 wt % and cross-linked via dynamic hydrazone bonds formed between hydrazine-modified ELP and HA functionalized with aldehyde (ALD) groups of varying reactivity (Fig. 1A). Specifically, we used benzaldehyde (BZA) to achieve slower bond exchange kinetics and an aliphatic ALD to achieve faster bond exchange kinetics. By modulating the ratio of BZA:ALD-functionalized HA (either 100:0 or 50:50), we developed hydrogels with similar shear storage moduli but distinct stress relaxation profiles, referred to here as Dyn Slow and Dyn Fast, respectively. Mechanical testing confirmed that, although both Dyn Slow and Dyn Fast HELP gels exhibited similar stiffness (~800 Pa, within the physiological range of brain tumors) (*34*, *35*) (Fig. 1B), they differed markedly in their ability to dissipate applied stress over time. The stress relaxation half-times ($\tau_{1/2}$) spanned from ~10^4 s for Dyn Fast to ~10^5 s for Dyn Slow gels (Fig. 1C). Although these rates are notably slower than that reported for native brain tissue (*36*), this material platform enables systematic exploration of how stress-relaxing microenvironments affect GBM cell behavior without confounding changes in stiffness or biopolymer composition. Both hydrogel formulations supported robust cell viability (>90%) upon encapsulation of the U-87 GBM cell line (fig. S1B), confirming the cytocompatibility of the system and establishing a reliable platform for downstream phenotypic analyses. Thus, the final HELP formulations mimic key compositional features of the diseased GBM niche, allowing for exploration of the impact of viscoelasticity while holding stiffness constant.

GBM cells were initially encapsulated within HELP hydrogels containing cell-adhesive ligands from both FBN and TNC proteins (termed FBN-TNC). Over 7 days, GBM cells exhibited markedly enhanced spreading and protrusive morphology in Dyn Fast compared to Dyn Slow matrices (Fig. 1D). To assess whether this viscoelasticity-dependent morphological response was limited to individually encapsulated cells or also manifested at the multicellular level, we preformed GBM spheroids and embedded them within HELP hydrogels. Immediately postencapsulation (day 0), spheroids retained their compact structure across both hydrogel types. However, by day 7, spheroids cultured in Dyn Fast hydrogels exhibited pronounced peripheral spreading and a loss of compactness, whereas those in Dyn Slow hydrogels preserved their initial spherical morphology while continuing to grow in size (Fig. 1E).

We next examined expression levels of P-selectin, a cell adhesion molecule traditionally associated with vascular endothelium and platelets. Although the role of P-selectin in GBM is still emerging, elevated P-selectin expression has been linked to aggressive behavior in several solid tumors, and therapies targeting P-selectin have shown substantial potential in preclinical GBM models, leading to their use in a current phase 1/2 clinical trial (NCT05909618) (*11*, *22*). Immunofluorescence analysis revealed consistently elevated P-selectin expression in GBM cells within Dyn Slow relative to Dyn Fast conditions (Fig. 1, F and G, and figs. S2 and S3). These observations were supported by quantitative reverse transcription polymerase chain reaction (qRT-PCR) analysis, which showed significantly higher *SELP* (the gene encoding P-selectin) transcript levels in cells cultured in Dyn Slow hydrogels (Fig. 1F). These results highlight that matrix viscoelasticity modulates both cell morphology and expression of invasion-associated markers.

Next, we investigated whether specific ECM biochemical signaling cues were required in our tumor-mimetic hydrogels. In particular, we leveraged the modularity of the HELP hydrogel platform to explore whether different cell-adhesive peptides would influence GBM morphology in dynamic matrices, comparing three HELP hydrogel formulations: FBN, FBN-TNC, and TNC (Fig. 2A). These formulations were engineered to have comparable stiffness (~800 Pa) and two different levels of stress relaxation kinetics, categorized as Dyn Slow or Dyn Fast (Fig. 2B). Characterization across different ligand conditions also demonstrated that peptide identity does not significantly alter bulk stiffness (Fig. 2B), confirming that stress relaxation is independently tuned in this system.

Immunofluorescence staining of P-selectin revealed that encapsulated GBM cells could sense and respond to matrix viscoelasticity regardless of changes in ligand identity (Fig. 2C). Across all hydrogel conditions, U-87 cells cultured in Dyn Slow hydrogels exhibited consistently higher P-selectin levels across all peptide configurations. Quantitative analysis confirmed this trend, with P-selectin intensity per cell significantly elevated in Dyn Slow matrices (Fig. 2D), whereas no significant differences were observed between the FBN, FBN-TNC, or TNC conditions within a given dynamic group. Similar results were obtained when U-87 cells were encapsulated in HELP hydrogels formulated with only the non-cell-adhesive, scrambled

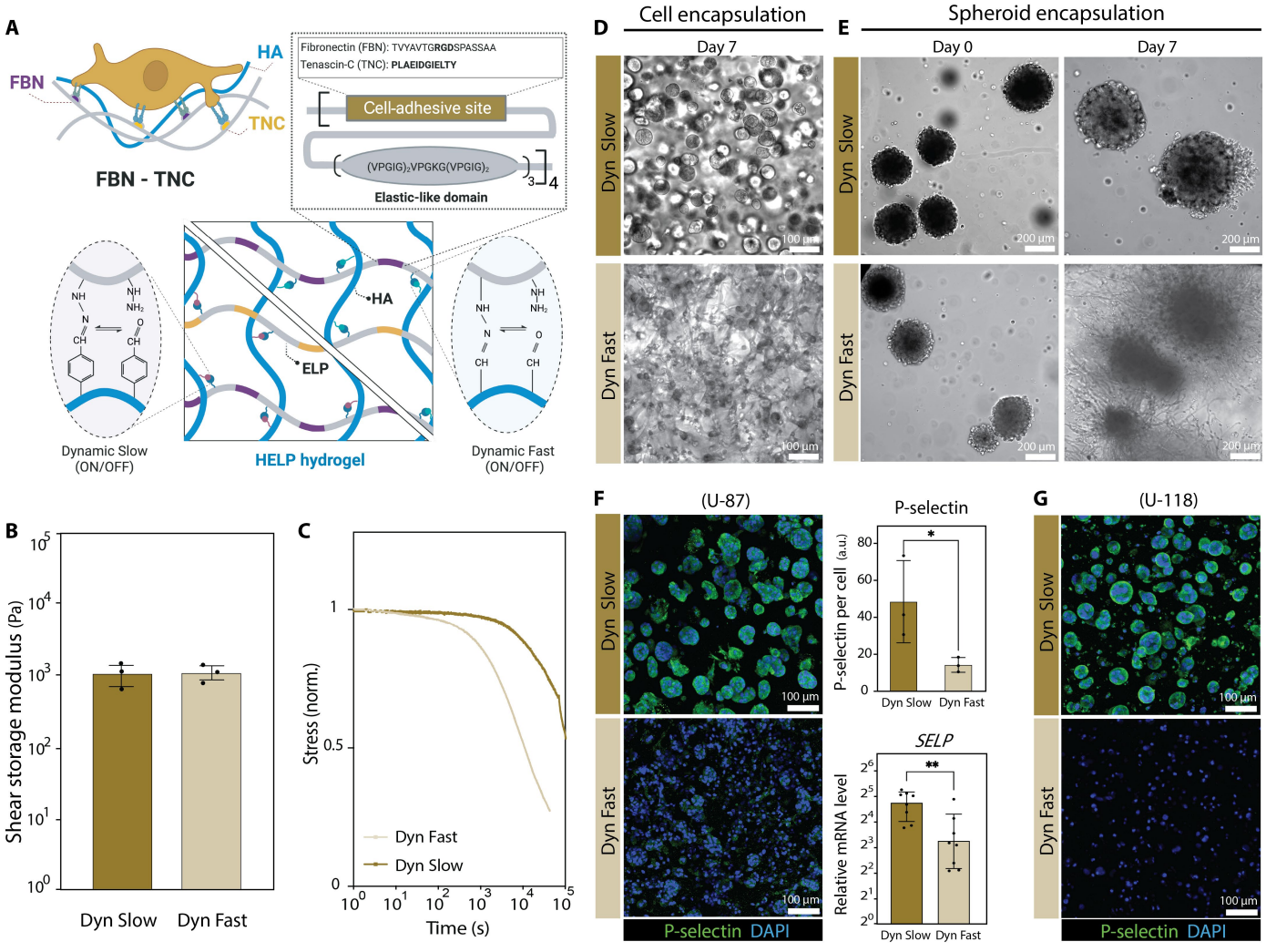

Fig. 1. Viscoelastic HELP hydrogels with ECM-mimetic motifs modulate GBM cell behavior. (**A**) Schematic of the HELP hydrogel integrating HA, ELPs, and dynamic cross-linkers to create tunable viscoelastic properties. Cell-adhesive peptides derived from FBN (RGD) and TNC (PLAEIDGIELTY) were incorporated in the backbone of ELPs. (**B**) Average shear storage moduli (G') of HELP hydrogels ($n = 3$) with slow (Dyn Slow) and fast (Dyn Fast) stress-relaxing dynamics. (**C**) Representative stress relaxation curves. (**D** and **E**) Bright-field images of U-87 cells that were initially encapsulated in HELP hydrogels as individual cells (D) or preformed spheroids (E). (**F**) Representative images of encapsulated U-87 cells immunostained for P-selectin (green) and counterstained for nuclei (DAPI; blue) at day 7 postencapsulation. Quantification of normalized P-selectin fluorescence per cell ($n = 6$ randomized fields of view; $N = 3$ replicate hydrogels; data are means ± SD, $^*P < 0.05$). a.u., arbitrary units. Expression level of normalized SELP (gene encoding P-selectin) mRNA relative to day 0 controls and normalized to the housekeeping gene after 7 days in Dyn Slow or Dyn Fast hydrogels ($N = 8$ replicate hydrogels; data are means ± SD, $^{**}P < 0.01$). Statistical analyses were two-tailed unpaired t tests. (**G**) Representative images of encapsulated U-118 cells stained for P-selectin (green) and nuclei (DAPI; blue) at day 7.

RDG protein (fig. S4, left). Thus, cells exhibited comparable P-selectin expression levels in Dyn Slow hydrogels with or without cell-adhesive peptides, suggesting that initial integrin-mediated adhesion is not required for P-selectin induction under these conditions.

Next, to assess whether P-selectin up-regulation in Dyn Slow hydrogels is dependent on receptor engagement with HA, we replaced HA in the HELP matrix with a bioinert polyethylene glycol (PEG) to form ELP-PEG hydrogels of matched stiffness and viscoelasticity (*37*, *38*). Within this PEG-based Dyn Slow system, we compared hydrogels functionalized with either the cell-adhesive FBN-derived RGD peptide or a nonadhesive scrambled RDG control. Notably, P-selectin expression remained unchanged across all conditions, suggesting that neither early HA-mediated signaling nor early integrin engagement was required for P-selectin induction under slow stress-relaxing conditions (fig. S4, right).

Matrix stress relaxation affects ECM remodeling and integrin expression in GBM cells

Given that matrix stress relaxation emerged as the dominant regulator of GBM cell behavior relative to ligand type, we focused our subsequent investigations on the role of viscoelasticity within HELP hydrogels presenting both FBN and TNC ligands. A previous work has demonstrated that changes in matrix stress relaxation rate can alter the ability of cells to remodel their surrounding environment by secreting new matrix proteins (*39*). Thus, although encapsulated cells are initially only exposed to cell-adhesive ligands presented by

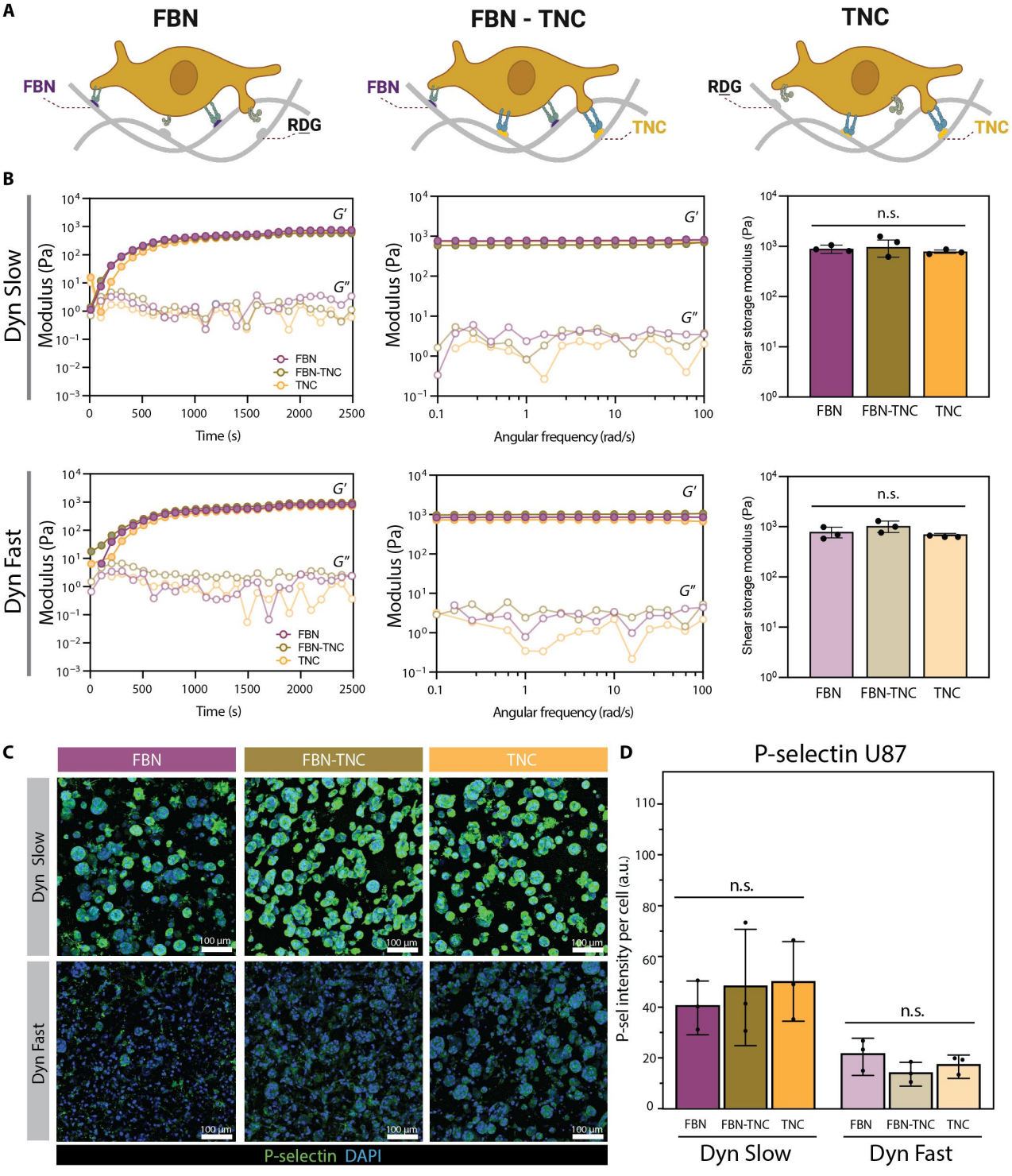

Fig. 2. Matrix stress relaxation affects P-selectin expression regardless of integrin ligands presented by the engineered hydrogel. (**A**) Schematic of three hydrogel formulations with varied integrin-binding peptide presentations: FBN, FBN-TNC, and TNC. (**B**) Rheological characterization of each formulation for Dyn Slow and Dyn Fast conditions. Time sweeps (left) show the increase in stiffness during cross-linking, whereas frequency sweeps of fully cross-linked gels (right) show consistent stiffness across peptide configurations ($G' \sim 800$ Pa). Storage moduli (G') are filled symbols, and loss moduli (G'') are open symbols. (**C**) Images of U-87 cells stained for P-selectin (green) and nuclei (DAPI; blue) at day 7 within Dyn Slow and Dyn Fast hydrogels with varied integrin-binding peptides. (**D**) Quantification of normalized P-selectin intensity per cell ($n = 3$ per group) for U-87 cells at day 7. Statistical analyses are one-way (B) or two-way (D) ANOVA with Tukey's multiple comparisons test.

the engineered hydrogel, over time they can produce their own adhesive matrix. To investigate how matrix viscoelasticity regulates ECM remodeling and integrin-mediated signaling in our GBM model, U-87 cells were encapsulated within 3D HELP hydrogels and compared with cells cultured on conventional 2D tissue-culture polystyrene (TCP). ECM remodeling was analyzed through a combination of immunostaining and transcriptional profiling of matrix components and integrin receptors. Immunofluorescence imaging revealed pronounced differences in FBN deposition across conditions (Fig. 3A). Cells cultured on 2D TCP formed flattened monolayers that grew horizontally to cover a large surface area, whereas cells cultured within 3D HELP hydrogels formed multicellular aggregates that were more compact. This is consistent with other published observations of GBM cell lines when grown within 3D hydrogels and could be due

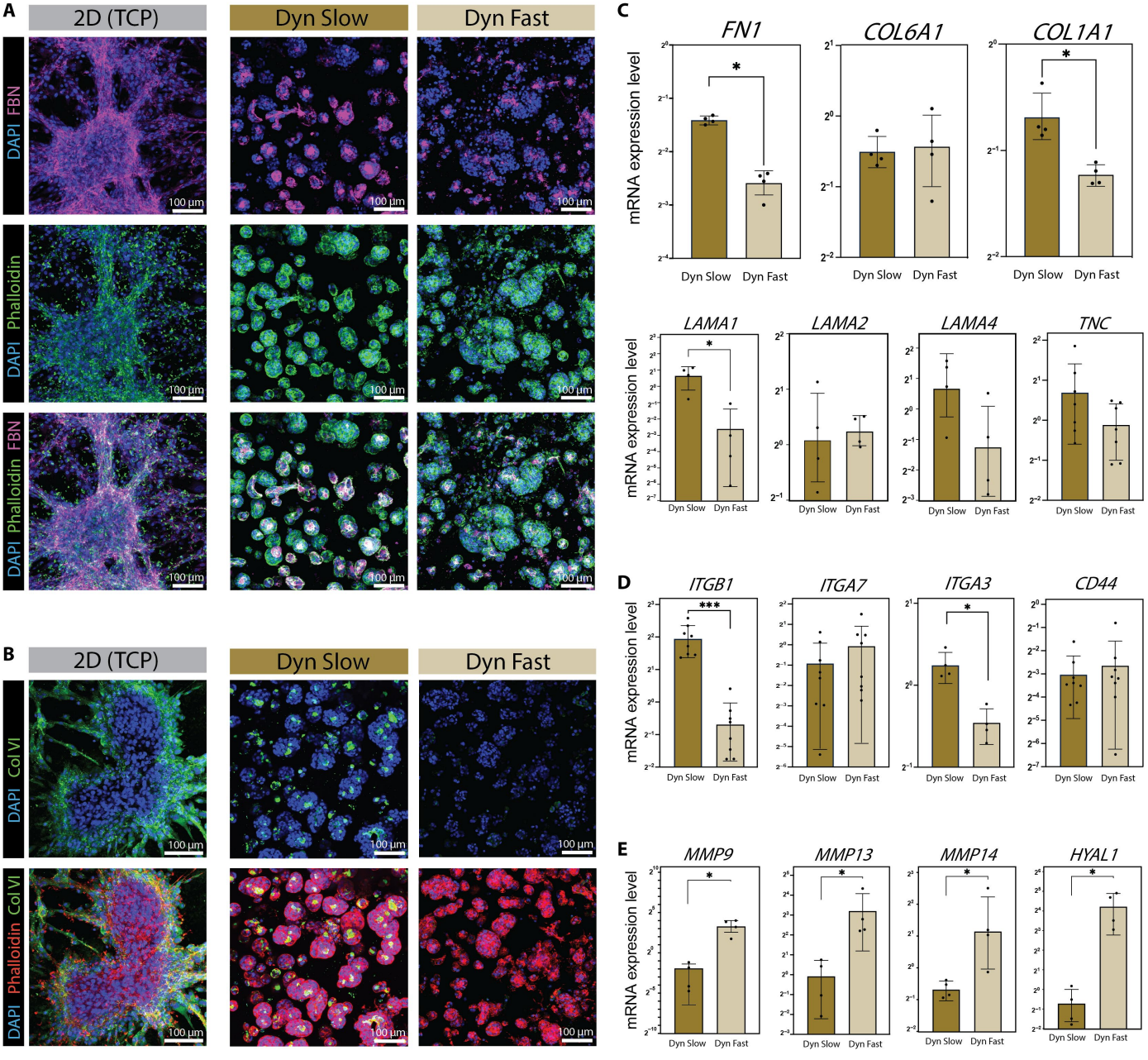

Fig. 3. Slow matrix stress relaxation enhances ECM remodeling and integrin-associated gene expression in GBM cells. (**A**) Representative images of FBN (magenta), F-actin (phalloidin; green), and nuclei (DAPI; blue) in U-87 cells cultured on 2D TCP or encapsulated in HELP hydrogels with either slow (Dyn Slow) or fast (Dyn Fast) stress relaxation rates for 7 days. (**B**) Representative images of ColVI (green), F-actin (phalloidin; red), and nuclei (DAPI; blue) in U-87 cells. (**C**) Quantitative real-time PCR analysis of ECM-related genes including FBN (*FN1*), ColVI (*COL6A1*), collagen I (*COL1A1*), laminin subunits (*LAMA1*, *LAMA2*, and *LAMA4*), and *TNC* for U-87 cells at day 7. (**D**) Gene expression of integrin subunits (*ITGB1*, *ITGA7*, and *ITGA3*) and *CD44*, a hyaluronan receptor, for U-87 cells at day 7. (**E**) Expression of matrix remodeling genes (*MMP9*, *MMP13*, and *MMP14*) and hyaluronidase (*HYAL1*) for U-87 cells at day 7. Expression levels were normalized to day 0 controls and housekeeping genes. Data represent means ± SD from $n \geq 4$ biological replicates. Statistical analyses are two-tailed unpaired *t* tests, $^*P < 0.05$.

to the spatial confinement provided by the 3D hydrogel and/or alterations in mass transport of cytokines and nutrients (*40*, *41*). On 2D TCP, the cells deposited nascent FBN and collagen VI (ColVI) mainly around the planar cell cluster margins. In contrast, cells embedded in Dyn Slow hydrogels secreted dense, pericellular FBN and ColVI, mainly in the core of 3D spheroid-like structures. In comparison, cells in Dyn Fast hydrogels exhibited dispersed morphologies and minimal ECM deposition (Fig. 3, A and B).

To evaluate whether these protein-level differences were reflected at the transcriptional level, we performed qRT-PCR analysis of key ECM genes after 7 days of encapsulation (Fig. 3C). GBM cells in Dyn Slow hydrogels exhibited significantly higher mRNA expression of FBN (*FN1*), ColVI alpha 1 (*COL6A1*), and collagen type I alpha 1 (*COL1A1*), indicating active matrix remodeling. These ECM proteins are commonly up-regulated in invasive GBM phenotypes and associated with chemoresistance in the in vivo tumor microenvironment (*42*, *43*). Expression of TNC, a known component of the GBM microenvironment up-regulated in perinecrotic and invasive regions, showed an upward trend in Dyn Slow hydrogels but did not reach statistical significance. Gene expression of laminin isoforms (*LAMA1*, *LAMA2*, and *LAMA4*) also exhibited modest increases under Dyn Slow conditions, consistent with the ECM deposition patterns observed in immunostaining (figs. S5 and S6). These results confirm that the stress relaxation properties initially presented by the engineered hydrogel support the activation of ECM-producing transcriptional programs in GBM cells.

We next investigated whether viscoelasticity altered expression of integrin receptors. U-87 cells in Dyn Slow hydrogels up-regulated expression of integrin subunit β1 (*ITGB1*) and integrin subunit α3 (*ITGA3*) (Fig. 3D), both of which facilitate cell-ECM adhesion and mechanotransduction in GBM progression (*44*, *45*). These integrins are known to enhance invasive behavior and therapy resistance when activated in mechanically stiff environments. Integrin subunit α7 (*ITGA7*), a laminin-binding integrin, showed no significant change, suggesting selective engagement based on mechanical context. *CD44* expression, a major receptor for HA (*46*), remained unaltered between Dyn Slow and Dyn Fast conditions (Fig. 3D). Together with our earlier findings that removal of HA from the hydrogel formulation did not affect P-selectin expression (fig. S4), these data imply that HA-*CD44* interactions are not a primary pathway mediating mechanotransduction of dissipative forces in our system.

Last, we assessed matrix remodeling enzyme expression in our GBM model (Fig. 3E). GBM cells in Dyn Fast hydrogels exhibited significantly elevated mRNA levels of matrix metalloproteinases (*MMP9*, *MMP13*, and *MMP14*) and hyaluronidase (*HYAL1*), enzymes involved in ECM degradation and remodeling. These results suggest that, whereas Dyn Slow environments promote ECM deposition, Dyn Fast matrices may signal cells to initiate ECM degradation.

These findings demonstrate that matrix stress relaxation influences the phenotypic behavior of GBM cells by modulating their ability to remodel the ECM and express integrin receptors for ECM engagement. The differential regulation of matrix deposition versus matrix degradation suggests that matrix viscoelasticity may modulate the balance between ECM assembly and turnover in GBM. These observations led us to hypothesize that slower-relaxing environments may preserve cytoskeletal tension and support the buildup of matrix-bound forces that favor ECM deposition, whereas faster-relaxing matrices dissipate cellular tension more rapidly, reducing mechanotransductive signaling and promoting ECM degradation.

Matrix stress relaxation regulates YAP1/β-catenin activation and cytoskeletal tension to control P-selectin expression

To evaluate whether matrix stress relaxation rate results in altered levels of cellular tension, we next investigated the potential mechanisms involved in mechanosignaling pathways. We focused on Yes-associated protein 1 (YAP1) and β-catenin, two central transcriptional coactivators that integrate mechanical cues with gene expression via cytoskeletal tension and cell-ECM adhesion dynamics (*47*). We first analyzed YAP1 expression as a canonical readout of mechanical signal transduction. In 2D culture on TCP, YAP1 expression was minimal (Fig. 4A). In contrast, cells cultured in Dyn Slow hydrogels displayed markedly higher YAP1 expression compared to those in Dyn Fast matrices, as evidenced by immunofluorescence and Western blotting. This response was consistent across U-87 and U-118 GBM cell lines (fig. S7), supporting the conclusion that YAP1 activation is a potential viscoelasticity-dependent phenomenon for GBM. In parallel, we analyzed the Wnt/β-catenin axis (*48*) and observed a similar pattern. Immunofluorescence imaging showed elevated levels of active (nonphosphorylated) β-catenin in Dyn Slow matrices relative to Dyn Fast (*49*) (Fig. 4B). At the transcriptional level, qRT-PCR analysis revealed significant up-regulation of CTNNB1 and down-regulation of its canonical downstream target AXIN2 under slow-relaxing conditions, implicating that matrix dissipative properties play a potential role in the activation of β-catenin–driven transcription.

Given the observed mechanosensitive activation of YAP1 and β-catenin, we next tested whether upstream regulation of cytoskeletal contractility through the RhoA-ROCK-myosin II axis was necessary for P-selectin up-regulation. To answer this, we treated encapsulated GBM cells with either a ROCK inhibitor (Y-27632) or a non-muscle myosin II inhibitor (blebbistatin) from days 7 to 10 postencapsulation. Both treatments markedly reduced P-selectin expression in Dyn Slow hydrogels, mimicking the phenotype of low P-selectin expression observed in Dyn Fast matrices (Fig. 4, C and D). These findings confirm that actomyosin-mediated cytoskeletal tension may be necessary for sustained P-selectin up-regulation in viscoelastic matrices.

Matrix stress relaxation regulates lipid metabolic states and protein expression profiles in GBM cells

Having identified that matrix stress relaxation modulates GBM mechanotransduction, ECM remodeling, and integrin expression, we next asked whether these mechanical cues influence other hallmarks of GBM. Among these, lipid metabolic reprogramming is increasingly recognized as a key driver of GBM proliferation, survival, invasion, and therapy resistance (*50*, *51*). GBM cells accumulate LDs not only as energy stores but also to shield cells from oxidative and metabolic stress within the tumor microenvironment, thereby enhancing survival and stemlike phenotypes (*52*–*54*). To examine how viscoelastic remodeling shapes GBM metabolic state, U-87 cells were cultured on 2D TCP or encapsulated in 3D HELP hydrogels (Dyn Slow versus Dyn Fast). At day 7, neutral lipid content was first visualized in bulk using Boron-dipyrromethene (BODIPY) dyes (Fig. 5A) and then further assessed by coherent anti-Stokes Raman scattering (CARS) microscopy (Fig. 5B). CARS microscopy, which detects CH_2 vibrational signatures, enables quantitative, label-free imaging of LDs in living cells and tissues (*55*, *56*). Our findings demonstrate that U-87 cells in Dyn Slow hydrogels exhibited a significantly higher LD count per cell compared to cells in Dyn Fast matrices (Fig. 5, A and B). One possible explanation is that Dyn Slow matrices sustain

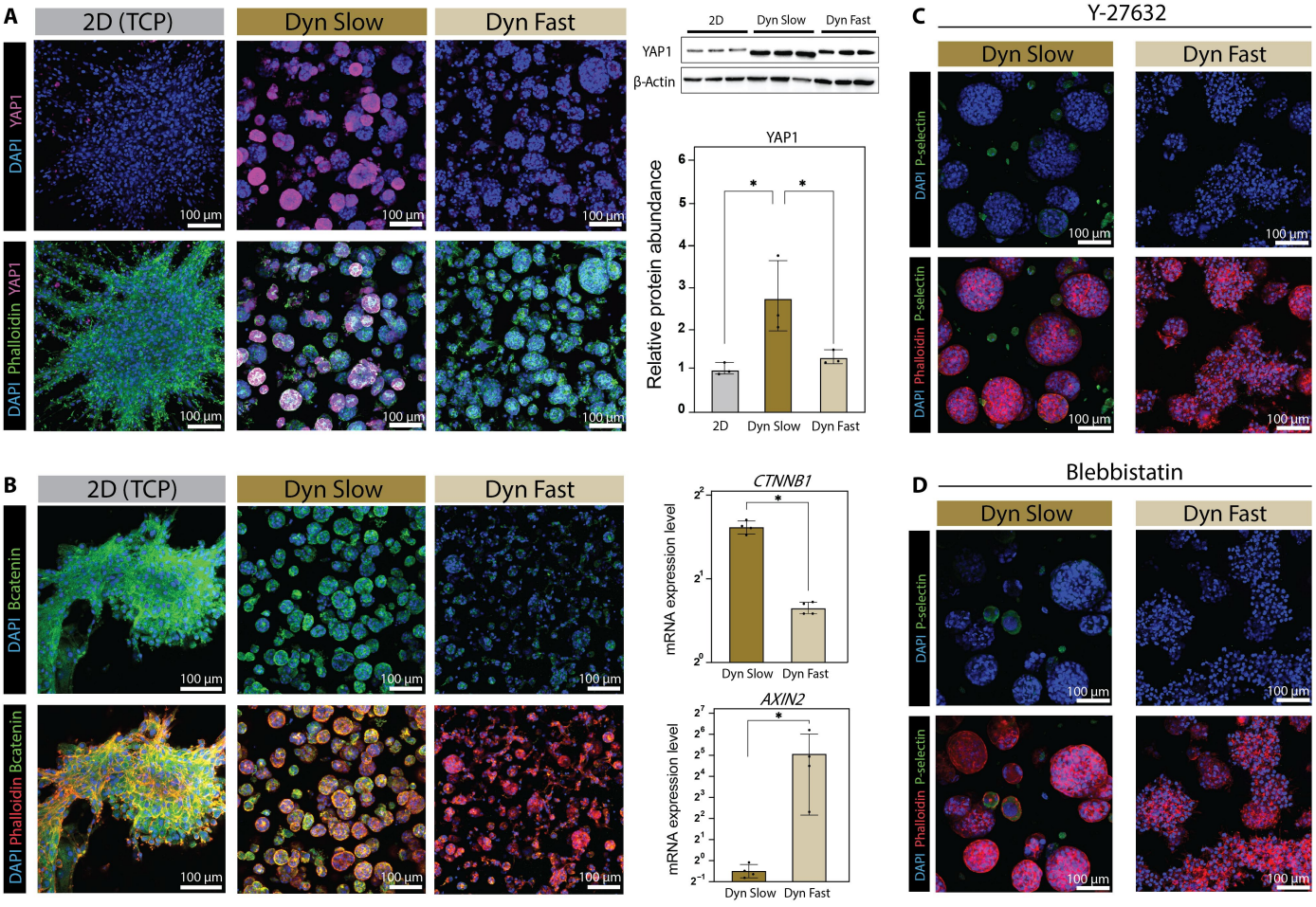

Fig. 4. Matrix stress relaxation regulates YAP/β-catenin activation and cytoskeletal tension to control P-selectin expression in GBM cells. (**A**) Left: Immunofluorescence of YAP1 (magenta) in U-87 cells cultured on 2D TCP or encapsulated in HELP hydrogels with slow (Dyn Slow) or fast (Dyn Fast) stress relaxation rates. Phalloidin (red) and DAPI (blue) stain F-actin and nuclei, respectively. Right: Western blot analysis of total YAP1 expression at day 7 normalized to β-actin. (**B**) Left: Immunofluorescence images of active (nonphospho) β-catenin (green) along with phalloidin (green) and DAPI (blue) staining. Right: Quantitative RT-PCR analysis of CTNNB1 (encoding β-catenin) and its downstream transcriptional target AXIN2 normalized to day 0 and the housekeeping gene. (**C** and **D**) Immunofluorescence of U-87 cells for P-selectin (green) expression along with phalloidin (red) and DAPI (blue) following treatment with either ROCK inhibitor Y-27632 (C) or actomyosin contractility inhibitor blebbistatin (D) at day 10. Data represent means ± SD, from $n = 3$ biological replicates; $^*P < 0.05$, by unpaired two-tailed t tests.

cytoskeletal tension and YAP/β-catenin signaling, which may enhance de novo lipogenesis and nucleation of new LDs, resulting in a larger number of droplets. This hypothesis is consistent with evidence that actomyosin-AMPK (*57*) and Hippo-YAP signaling can promote LD biogenesis (*58*).

Moreover, mechanical forces are also known to regulate secretory programs that shape tumor-stroma communication (*59*). Thus, we next examined whether matrix viscoelasticity alters the cytokine and protein expression landscape in GBM cells. Day 7 cell lysate analysis (Fig. 5C and fig. S8) revealed distinct expression profiles of secreted proteins among the different experimental groups. Dyn Slow cultures showed elevated macrophage inhibitory factor (MIF) and ECM metalloproteinase inducer (EMMPRIN, also known as CD147), molecules implicated in GBM tumorigenesis, immune modulation, and MMP induction, respectively (*60*–*63*). In contrast, GBM cells in Dyn Fast hydrogels preferentially up-regulated transferrin receptor (TfR), chitinase-3-like protein 1 (CHI3L1, also known as YKL-40), and osteopontin, proteins associated with GBM invasion or stemness (*64*–*68*). Moreover, interleukin-8 (IL-8) levels were higher under the Dyn Fast condition, consistent with its role in promoting GBM invasion and cell migration (*69*–*71*), along with increased SERPINE1 expression, suggested to drive GBM dispersal (*72*).

DISCUSSION

Our data establish that GBM cell lines are responsive to matrix stress relaxation kinetics (at similar matrix stiffness), which correlates with altered expression of adhesion molecules (P-selectin), ECM remodeling, mechanotransduction (YAP/β-catenin), lipid storage, and cytokine/protein expression. This finding is consistent with foundational mechanobiology studies showing that matrix stress relaxation, independent of bulk stiffness, can govern cell spreading, contractility, and fate decisions for multiple cell types (*9*, *73*). Although the matrix stress relaxation rates studied here are slower than that reported for whole brain tissue and GBM tumors (*6*, *73*), this range of dissipative kinetics is known to alter the phenotype of other cells in the nervous

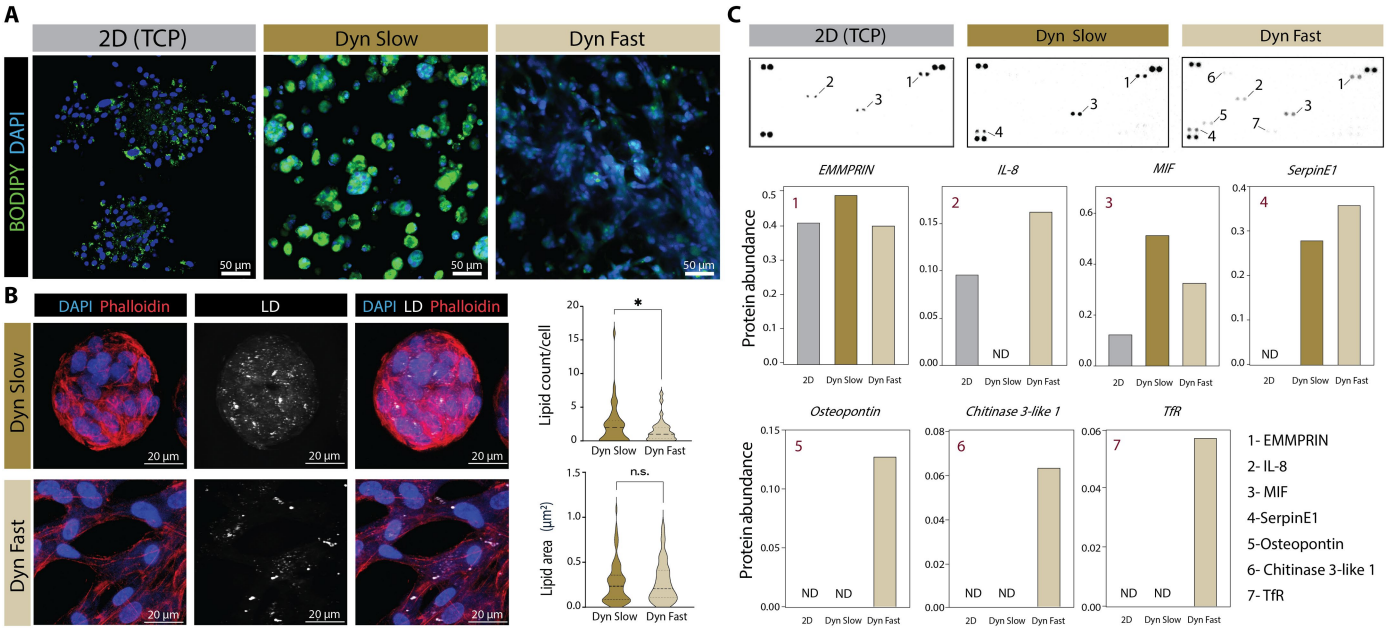

Fig. 5. Matrix stress relaxation modulates LD accumulation and protein expression in GBM cells. (**A**) BODIPY staining of LD in U-87 cells cultured on 2D TCP or encapsulated in Dyn Slow or Dyn Fast HELP hydrogels. (**B**) Left: Merged CARS and immunofluorescence images of LD along with phalloidin (red) and DAPI (blue) staining. Right: Quantification of LD count per cell and individual LD area for U-87 cells at 7 days postencapsulation. Statistical analyses are two-way ANOVA with Tukey's multiple comparisons test. (**C**) Cytokine/protein antibody array analysis of U-87 cell lysates collected at day 7 from 2D, Dyn Slow, and Dyn Fast cultures. Representative array membranes (top) and semiquantitative bar graphs (bottom) depict relative protein abundance. ND, not detected.

system (*21*, *24*, *74*, *75*). A number of strategies have been reported to alter the viscous dissipation kinetics of biomaterial hydrogels (*76*–*78*), and future studies could further expand the range of viscoelastic mechanical properties.

In our system, slower-relaxing (Dyn Slow) HELP hydrogels favored tension-dependent phenotypes across multiple readouts, whereas faster-relaxing (Dyn Fast) gels attenuated those responses. Most notably, GBM cells responded to this mechanosignaling through regulation of P-selectin expression. We observed higher *SELP* expression in Dyn Slow versus Dyn Fast across GBM cell lines and in several different matrix formulations, with pharmacologic reduction upon inhibition of cytoskeletal tension. P-selectin is best known for its role in capturing leukocytes within the bloodstream, where hemodynamic forces initiate downstream P-selectin activity (*79*). In cancer, P-selectin is up-regulated on tumor endothelium, where it mediates cancer cell metastasis through the blood stream (*80*). P-selectin–targeted nanomedicines are suggested to enhance vascular docking and to enable active blood-brain-barrier transcytosis in brain tumors, thereby improving intratumoral delivery (*80*, *81*). More recently, P-selectin was discovered to be significantly up-regulated on GBM cells in vivo compared to healthy brain tissue, enabling dual targeting (*22*). In preclinical models, P-selectin dual targeting of GBM resulted in significant improvements in animal survival (*22*). Future work will be required to extend our studies to patient-derived cells for evaluation of the time-course and mechanistic pathways responsible for mechanosignaling-mediated P-selectin expression. As a first step toward mechanistic understanding, our findings suggest the involvement of YAP and β-catenin signaling. This is consistent with evidence suggesting that YAP/TAZ are effectors of matrix-dependent tension and mediate cross-talk with Wnt/β-catenin (*82*, *83*).

GBM cell response to matrix stress relaxation rate did not require the initial presentation of a particular integrin-binding motif nor the presence of HA in our model. In contrast, cells enacted different matrix remodeling programs in response to the initial matrix mechanics. Dyn Slow promoted deposition and transcriptional up-regulation of FBN (*FN1*) and collagens (e.g., *COL6A1*), whereas Dyn Fast induced matrix degradation mechanisms through up-regulation of matrix-degrading enzymes (*MMP9*, *MMP13*, *MMP14*, and *HYAL1*). Clinical and experimental findings demonstrate GBM frequently shows enriched FBN, TNC, and collagen isoforms that support adhesive migration and immune modulation (*84*, *85*). Col-VI, in particular, can be produced by GBM cells to prime invasion, correlating with poorer outcomes (*86*). Consistent with our integrin data, other studies show that α3 and β1 integrin subunits contribute to glioma invasion, therapy resistance, and vascular interactions (*87*–*90*). Although other evidence suggests that the HA-CD44 axis can influence GBM invasion (*91*, *92*), in our model, CD44 transcript levels were unchanged. Given these phenotypic shifts in matrix remodeling, future in vitro models would benefit from real-time analyses of changes in matrix viscoelasticity (*93*, *94*).

We also observed correlations between matrix stress relaxation rate and GBM lipid metabolism. Using BODIPY for bulk LD detection and label-free CARS microscopy for single-cell quantification, we found that Dyn Slow was characterized by more LDs per cell, whereas Dyn Fast showed fewer LDs of similar size. Actomyosin and Hippo-YAP signaling are potential regulators of lipid metabolism in several systems (*95*–*97*). In GBM specifically, lipid metabolism and LD accumulation support malignancy and therapeutic vulnerabilities (*50*, *51*). In our platform, the increased abundance of LDs under Dyn Slow conditions may represent a stress-protective response within a

mechanically confining niche. These data support future efforts at metabolomic analyses in GBM in vitro models.

Last, our immunoassays on cell lysates revealed viscoelasticity-dependent expression programs. In Dyn Fast hydrogels, GBM cells had elevated expression levels of TfR, CHI3L1, osteopontin, IL-8, and SERPINE1, suggestive of proinvasive chemokine signaling and migratory GBM dispersal. This notion is consistent with the up-regulation of matrix-degrading enzymes and the elongated morphological structures observed in Dyn Fast hydrogels. On the other hand, in Dyn Slow, elevated MIF and EMMPRIN were notable. MIF promotes endothelial adhesive function and P-selectin–dependent leukocyte rolling in vivo, and EMMPRIN is reported to trigger platelet degranulation and increased expression of P-selectin (*98*, *99*). These findings correlate with higher expression of P-selectin in Dyn Slow, suggesting that up-regulation of several P-selectin–related genes may be coordinated to regulate cell-adhesive interactions involved in GBM progression.

Notably, our current in vitro model includes only GBM cells and an engineered matrix. In addition, this study uses immortalized GBM cell lines (U-87 and U-118), which, although well characterized and reproducible, do not fully capture the interpatient heterogeneity of GBM. These two cell lines were selected in part due to their distinct phenotypic characteristics, including differences in morphology, invasiveness, and molecular profiles (*100*), enabling an initial assessment of whether viscoelasticity-dependent responses are replicated across different GBM models. Although consistent trends were observed across both lines, future studies using patient-derived GBM cells will be essential to determine how matrix viscoelasticity influences tumor behavior across clinically relevant subtypes.

Although the HELP platform incorporates key components of the brain ECM, including HA and ECM-derived ligands, it remains a simplified system that does not fully capture the cellular and biochemical complexity of the tumor microenvironment. This level of control is essential for isolating the cause-and-effect relationships between matrix properties and GBM cells. However, this strategy does not capture the multitude of other interactions occurring in the tumor microenvironment with the diverse other cell types that are present in vivo. As P-selectin is specifically hypothesized to mediate GBM cell interactions with the endothelium and microglia (*23*), future studies could expand the model complexity by incorporating additional cell types.

In summary, our data indicate that the matrix stress relaxation rate, at matched stiffness and independent of initial cell-adhesive ligand presentation, is a key parameter that regulates GBM morphology, ECM remodeling, mechanotransduction, lipid metabolism, and cell-intrinsic protein programs (Fig. 6). Slow-relaxing hydrogels, which retain cellular traction over time, are associated with enhanced ECM deposition, accumulation of LDs, and elevated expression of P-selectin and potential mediators such as MIF and EMMPRIN that may reinforce adhesive-inflammatory signaling. In contrast, fast-relaxing matrices favor ECM-degradative signatures, fewer LDs, and enrichment of proteins associated with invasion (TFRC, CHI3L1, osteopontin, IL-8, and SERPINE1). These findings underscore matrix stress relaxation as a considerable regulator of GBM cell state and establish HELP hydrogels as a platform for probing biomechanical and biochemical influences on tumor biology. This tunable in vitro system enables reductionist modeling of the GBM microenvironment and supports the discovery of mechanosensitive pathways with therapeutic potential.

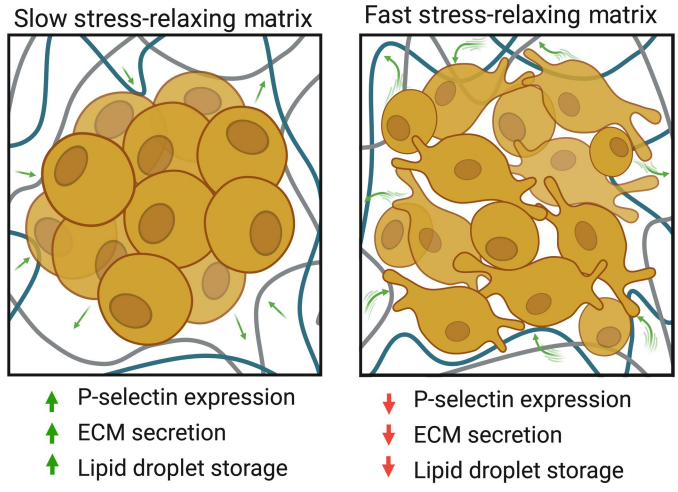

Fig. 6. Schematic of the matrix viscoelasticity modulation of GBM phenotypes. In engineered hydrogels with slower stress relaxation rates (**left**), a spheroidal morphology is maintained and is accompanied by elevated P-selectin expression, enhanced matrix deposition, and LD accumulation. Conversely, in hydrogels with faster stress relaxation (**right**), enhanced cell spreading is observed together with reduced expression of P-selectin, expression of matrix-degrading enzymes, and limited LD storage, suggesting a migratory phenotype.

MATERIALS AND METHODS

ELP expression, purification, and characterization

ELPs bearing cell-adhesive ligands derived from FBN (RGD), TNC (PLAEIDGIELTY), or nonadhesive scrambled ligand (RDG) motifs were recombinantly expressed and purified according to our established protocols (*101*). Briefly, *Escherichia coli* [either BL21(DE3) pLysS for the RGD and RDG variants or BL21 Star (DE3) pLysS for the PLAEIDGIELTY variant (Invitrogen)] were transformed with a pET15b plasmid encoding the desired ELP sequence. Individual transformed colonies were selected and initially cultured overnight in sterile Terrific Broth (Thermo Fisher Scientific), supplemented with 0.4% glycerol and ampicillin (100 μg/ml), at 37°C.

For the RGD and RDG variants, the following day, 20 ml of the overnight culture was transferred into 1 liter of the same growth medium in baffled flasks. Cultures were maintained at 37°C with continuous shaking until reaching an optical density ($\lambda = 600$ nm) of 0.6, after which the temperature was reduced to 32°C. Upon reaching an optical density ($\lambda = 600$ nm) of 0.8, protein expression was induced by the addition of 1 mM isopropyl-β-D-thiogalactopyranoside (IPTG; Thermo Fisher Scientific), and cells were incubated for an additional 7 hours. For the PLAEIDGIELTY variant, protein expression occurred at 25°C for 24 hours.

Cells were harvested by centrifugation, resuspended in TEN buffer [10 mM Tris, 1 mM EDTA, and 100 mM NaCl (pH 8.0)], and stored at −80°C. Cell lysis was achieved through three freeze-thaw cycles, followed by treatment with 10 μM deoxyribonuclease I (Sigma-Aldrich) and 1 mM phenylmethylsulfonyl fluoride (PMSF; Thermo Fisher Scientific) to degrade nucleic acids and inhibit protease activity, respectively.

Purification of ELPs was performed via three sequential rounds of thermal cycling. In each cycle, the pH of the sample was first adjusted to 9.0, followed by a cold centrifugation step (15,000*g*, 4°C, 1 hour) to remove insoluble debris. The clarified supernatant was then supplemented with salt (1 M sodium chloride for the RGD and

RDG variants or 1 M ammonium sulfate for the PLAEIDGIELTY variant) and incubated at 37°C for 3 hours to trigger ELP aggregation. A subsequent hot spin (15,000*g*, 37°C, 1 hour) was used to collect the aggregated ELP, which was redissolved in ultrapure water and allowed to dissolve overnight at 4°C. After three cycles of this purification process, a final cold spin was conducted to remove residual insoluble material. The supernatant was then dialyzed against ultrapure water for 72 hours using 10-kDa molecular weight cutoff (MWCO) dialysis tubing and lyophilized for storage at −20°C.

Synthesis of hydrazine-modified ELP

Hydrazine functionalization of ELPs was carried out as previously described (*102*). Lyophilized ELP was first dissolved at 7.3% (w/v) in anhydrous dimethyl sulfoxide (DMSO; Sigma-Aldrich) at room temperature (RT). After complete dissolution, an equal volume of anhydrous *N*,*N*′-dimethylformamide (DMF; Sigma-Aldrich) was added to the solution. Separately, tri-Boc-hydrazinoacetic acid (2.1 equiv per primary amine on the ELP; Sigma-Aldrich) and hexafluorophosphate azabenzotriazole tetramethyl uronium (HATU; 2 equiv per ELP amine; Sigma-Aldrich) were dissolved in the same volume of anhydrous DMF. Following dissolution, 4-methylmorpholine (5 equiv per ELP amine; Sigma-Aldrich) was added, and the mixture was allowed to react for 10 min at RT. The activated hydrazine solution was then added dropwise to the ELP-containing solution, and the reaction proceeded overnight at RT with constant stirring. The following day, the reaction mixture was precipitated using ice-cold diethyl ether (Thermo Fisher Scientific), and the resulting product was collected by centrifugation and dried under nitrogen to obtain butoxycarbonyl (Boc)–protected hydrazine-modified ELP. To deprotect the Boc groups, the dried material was resuspended in a 1:1 mixture of dichloromethane (DCM; Sigma-Aldrich) and trifluoroacetic acid (TFA; Sigma-Aldrich), containing 5% (v/v) triisopropylsilane (Sigma-Aldrich) as a scavenger. The solution was stirred at RT for 4 hours in a vented container. The final hydrazine-functionalized ELP was obtained by precipitation in cold ether, pelleting by centrifugation, and drying under nitrogen. The pellet was redissolved in ultrapure water, dialyzed using 10-kDa MWCO tubing for 3 days, and subsequently sterile filtered, lyophilized, and stored at −20°C.

Synthesis of BZA- and ALD-functionalized HA

BZA- and ALD-modified HA derivatives were synthesized in a two-step process involving initial carbodiimide coupling followed by copper-catalyzed azide-alkyne (CuAA) click chemistry as previously described (*74*). In the first step, 100-kDa sodium hyaluronate (LifeCore) was functionalized with propargylamine to introduce terminal alkyne groups. HA was dissolved at 1% (w/v) in MES buffer [0.2 M MES hydrate (Sigma-Aldrich) and 0.15 M NaCl (pH 4.5)] and stirred at RT. Propargylamine (0.8 equiv per HA dimer unit; Sigma-Aldrich) was added, and the solution pH was immediately adjusted to 6.0. *N*-Hydroxysuccinimide (NHS; 0.8 equiv per HA dimer unit; Thermo Fisher Scientific) and 1-ethyl-3-(3-dimethylaminopropyl) carbodiimide hydrochloride (EDC; 0.8 equiv per HA dimer unit; Thermo Fisher Scientific) were then sequentially added to activate the HA carboxyl groups. The reaction proceeded overnight under constant agitation. The resulting HA-alkyne was purified by dialysis (10-kDa MWCO) against ultrapure water for 3 days, sterile filtered, lyophilized, and stored at −20°C.

In the second step, the conjugation of BZA and ALD functional groups occurred through a subsequent CuAA click chemistry reaction. Briefly, lyophilized HA-alkyne was dissolved at 1% (w/v) in 10× isotonic phosphate-buffered saline [PBS; 81 mM Na_2HPO_4, 19 mM NaH_2PO_4, and 60 mM NaCl (pH 7.4)] containing β-cyclodextrin (1 mg/ml; Sigma-Aldrich) at RT. After degassing under nitrogen for 30 min, degassed solutions of sodium ascorbate (4.52 mM; Sigma-Aldrich) and copper(II) sulfate pentahydrate (0.24 mM; Sigma-Aldrich) were sequentially added to catalyze the reaction. For BZA functionalization, an azidobenzaldehyde derivative (2 equiv per alkyne group; synthesized as previously described (*37*)] was dissolved in anhydrous DMSO and added to the reaction vessel. For ALD functionalization, Ald-CH_2-PEG_3-azide (2 equiv per alkyne group; BroadPharm) was directly introduced. After an additional 10-min degassing, the reaction proceeded for 24 hours at RT in the dark under constant stirring. To terminate the reaction and chelate residual copper ions, an equal volume of 50 mM EDTA (pH 7.0) was added and incubated for 1 hour. The final product was then dialyzed against ultrapure water (10-kDa MWCO) for 3 days, sterile filtered, lyophilized, and stored at −20°C until use.

Formation of dynamic HELP hydrogels

Lyophilized ELP and HA were each reconstituted in 10× isotonic PBS to a final concentration of 2% (w/v) and allowed to dissolve overnight at 4°C. Once fully solubilized, solutions were stored on ice until use. Later, 5 μl of HA solution was first pipetted into custom-fabricated silicone molds [4 mm (diameter) by 0.8 mm (height)] that had been plasma bonded to 12-mm circular #2 glass coverslips (Electron Microscopy Sciences) and chilled on ice. An equal volume (5 μl) of ELP solution was then added directly to the mold and manually mixed in circular motions using the same pipette tip to initiate in situ cross-linking. Polymerization proceeded by incubating the gels for 15 min at RT, followed by 10 min at 37°C.

Measuring hydrogel rheological properties

Shear rheology was conducted using a stress-controlled AR-G2 rheometer (TA Instruments) equipped with a 20-mm diameter cone-on-plate geometry (1° cone angle). HELP hydrogel samples (48 μl) were prepared directly on the rheometer stage. To prevent dehydration during measurement, a layer of heavy mineral oil was applied around the sample periphery.

Hydrogels were allowed to complete cross-linking in situ on the rheometer stage under a controlled oscillatory strain (1%) and angular frequency (1 rad/s) for 15 min at 23°C, followed by an additional 15-min incubation at 37°C. To assess the final elastic properties of the hydrogels, a frequency sweep was performed from 0.1 to 100 rad/s under 1% oscillatory strain at 37°C. The storage moduli (G') reported correspond to measurements at 1 rad/s. To evaluate viscoelastic behavior, stress relaxation tests were performed by applying a constant 10% shear strain, and the resulting stress decay was recorded over 24 hours at 37°C. The characteristic relaxation time ($\tau_{1/2}$) is defined as the time required for the stress to decay to 50% of its initial value. All rheological data were acquired using the TRIOS software (TA Instruments).

GBM cell culture

U-87 MG and U-118 MG human GBM cell lines were obtained from the American Type Culture Collection (ATCC). Cells were maintained in Dulbecco's modified Eagle's medium (DMEM; Life Technologies) supplemented with 10% fetal bovine serum (FBS; Gibco), penicillin (100 U/ml), and streptomycin (100 μg/ml). Cultures were

kept in a humidified incubator at 37°C with 5% CO_2. For hydrogel encapsulation, cells were detached using trypsin, collected by centrifugation, and resuspended in fresh media for counting. The final pellet was then mixed into a 2% (w/v) ELP precursor solution at twice the target cell concentration (e.g., 1×10^4 cells/μl to yield a final density of 5×10^3 cells/μl following gelation). HELP hydrogels were formed as described above, and each silicon mold containing 10-μl gels was placed into an individual well of a 24-well plate. A total of 1 ml of culture medium was added to each well and exchanged with fresh media every other day.

For spheroid experiments, U-87 aggregates were formed using the AggreWell 800 platform (STEMCELL Technologies) following the manufacturer's guidelines. Preformed spheroids were collected, counted, and gently transferred into the HELP hydrogels before cross-linking to achieve uniform encapsulation within matrices.

Viability assays

To evaluate cell viability within the HELP hydrogels, GBM-encapsulated hydrogels were incubated in PBS containing 2 μM calcein-AM and 4 μM ethidium homodimer-1 (Invitrogen) for 10 min at 37°C. Following staining, hydrogels were gently washed with PBS to remove unbound dyes and immediately imaged using a laser scanning confocal microscope (Leica SPE, Las-X software). *Z*-stack images were acquired to capture 3D viability profiles, and live/dead quantification was performed from maximum intensity projections.

Immunocytochemistry

GBM-laden HELP hydrogels were fixed in 4% paraformaldehyde (PFA) in PBS at RT for 20 min, followed by three PBS washes. Fixed samples were stored at 4°C until staining. For permeabilization, constructs were incubated in 0.25% (v/v) Triton X-100 in PBS (PBS-T) for 1 hour at RT under gentle rocking. Nonspecific binding was blocked by incubating samples for 2 hours at RT in a blocking buffer consisting of 5% (w/v) bovine serum albumin (BSA; Roche), 5% (v/v) goat serum (Gibco, 16210064), and 0.5% (v/v) Triton X-100 (Sigma-Aldrich, T8787) in PBS.

Primary antibodies were applied to the samples and incubated overnight at 4°C with gentle rocking at the following dilutions: rabbit anti-P-selectin (1:300, Invitrogen, 3H20L10), rabbit anti-COL6A1 (1:400, Proteintech,17023-1-AP), rabbit anti-laminin (1:300, Invitrogen, PA1-16730), rabbit anti-YAP1 (1:400, Invitrogen, PA1-46189), rabbit anti-nonphospho (active) β-catenin (1:300, Cell Signaling Technology, 8814), and mouse anti-fibronectin (1:400, Proteintech,1G10F9). After primary incubation, samples were washed three times with PBS-T for 10 min each at RT. Secondary antibodies were prepared in an antibody dilution buffer and included: goat anti-rabbit Alexa Fluor 488 (1:500, Invitrogen, A-11008) and goat anti-mouse Alexa Fluor 594 (1:500, Invitrogen, A-11032). Samples were incubated with the secondary antibody solution overnight at 4°C with gentle rocking. 4′,6-Diamidino-2-phenylindole (DAPI; 1 μg/ml, Cell Signaling Technology, 4083s) and phalloidin (Sigma-Aldrich) were included in the secondary antibody solution to stain nuclei and F-actin, respectively. Samples were incubated overnight at 4°C with gentle rocking. Following incubation, hydrogels were washed three times with PBS-T for 20 min each and then mounted onto no. 1 coverslips using the ProLong Gold Antifade Mountant (Thermo Fisher Scientific). After 24 hours of curing at RT, samples were imaged using a Leica SPE confocal microscope. All images were acquired at *z*-depths ≥ 50 μm from the coverslips to avoid possible confounds imparted by the mechanical properties of the glass.

Quantitative reverse transcription polymerase chain reaction

For qRT-PCR, total RNA was extracted from encapsulated GBM cells following enzymatic hydrogel degradation. HELP hydrogels were transferred to microcentrifuge tubes and incubated with an equal volume of PBS containing hyaluronidase (2000 U/ml) and elastase (250 U/ml) for 30 min at 37°C to enzymatically digest the hydrogel matrix. Following digestion, cell suspensions were lysed in TRIzol reagent (Invitrogen) and stored at −80°C until RNA extraction.

Before RNA isolation, samples were thawed on ice and homogenized using a probe sonicator (Heilscher UP50H) at 50% amplitude (25 W), 30-kHz frequency, with a 0.5-s on/off cycle. mRNA was purified using an mRNA isolation kit (Zymo Research) according to the manufacturer's protocol. Following two washes with 70% ethanol, RNA pellets were air dried and resuspended in nuclease-free water. cDNA synthesis was performed using 100 ng of purified RNA with the high-capacity cDNA reverse transcription kit (Applied Biosystems). Synthesized cDNA was diluted 1:10 in nuclease-free water. For each qRT-PCR reaction, 6.6 μl of diluted cDNA was mixed with 0.9 μl of a 5 μM forward and reverse primer pair solution and 7.5 μl of Fast SYBR Green Master Mix (Applied Biosystems), in a total volume of 15 μl. Reactions were performed using a StepOnePlus Real-Time PCR System (Applied Biosystems), and data were analyzed using the ΔCT method, with expression levels normalized to the housekeeping genes GAPDH or ACTB. Primer sequences are listed in table S1.

Western blotting

For Western blotting, encapsulated GBM cells were first released from HELP hydrogels using enzymatic degradation as described above. Following digestion, cells were pelleted by centrifugation, and the supernatant containing hydrogel remnants was discarded. The cell pellets were resuspended in radioimmunoprecipitation assay (RIPA) lysis buffer (Thermo Fisher Scientific) supplemented with 1 mM PMSF and a protease inhibitor cocktail (Roche). The samples were incubated on ice for 20 min and stored at −80°C until use.

Before electrophoresis, lysates were thawed on ice, mixed with 5× gel loading buffer (300 mM Tris at pH 6.8, 50% glycerol, 10 wt % SDS, and 0.05 wt % bromophenol blue) supplemented with 500 mM dithiothreitol (DTT), and boiled at 95°C for 10 min. Protein samples were resolved on 12% precast SDS–polyacrylamide gel electrophoresis gels (Bio-Rad) and transferred to polyvinylidene difluoride membranes (Invitrogen) by wet transfer at 100 V for 70 min. Membranes were cut to enable staining of different molecular weight proteins from the same gel and blocked in 5% nonfat dry milk for 1 hour at RT.

Blots were incubated overnight at 4°C in the following primary antibodies diluted in 5% milk in tris-buffered saline (TBS-T) [20× stock: 3 M NaCl and 750 mM tris-HCl (pH 7.2)] supplemented with 0.25% (v/v) Tween 20: rabbit anti-YAP1 (1:400, Invitrogen, PA1-46189) and rabbit anti-nonphospho (active) β-catenin (1:300, Cell Signaling Technology, 8814). The following day, membranes were washed three times with TBS-T (5 min each) and incubated with horseradish peroxidase-conjugated secondary antibodies (Jackson ImmunoResearch) diluted in TBS-T for 1 hour at RT. After four additional 10-min washes in TBS-T, membranes were developed using

SuperSignal West Pico or Femto chemiluminescent substrates (Thermo Fisher Scientific) and imaged on a ChemiDoc MP gel imaging system (Bio-Rad). Band intensities were quantified using the Image Lab software (Bio-Rad), and representative blots from three independent biological replicates are reported.

Inhibitor treatments

To perturb ROCK signaling and cytoskeletal tension by inhibiting the activity of myosin II, U-87 GBM cells encapsulated in HELP hydrogels were treated with Y-27632 (100 μM; Tocris Bioscience, 1254) and blebbistatin (100 μM; Tocris Bioscience, 1852), respectively. DMSO served as the vehicle control. Treatments were administered from day 7 to day 10 post-encapsulation, at which point analyses were performed.

Secretome antibody array

To analyze the secreted protein profile of GBM cells, we used the Human XL Cytokine Array Kit (R&D Systems) in accordance with the manufacturer's protocol. Cell lysates were collected from U-87 GBM cells cultured for 7 days either on conventional 2D TCP or within our 3D HELP hydrogels. Lysates were diluted and incubated overnight with nitrocellulose membranes precoated with antibodies targeting 105 cytokines and tumor-related signaling proteins. Following incubation, membranes were thoroughly washed and treated with a mixture of biotinylated detection antibodies, followed by streptavidin-conjugated horseradish peroxidase. Signal detection was performed using a chemiluminescent substrate, and images were acquired using a ChemiDoc MP gel imaging system (Bio-Rad). Spot intensities corresponding to protein abundance were quantified using the ImageJ software, and only proteins exhibiting differential expression between conditions were reported. Protein array analysis was performed using one membrane per condition. Each target protein is represented by duplicate spots on the membrane, which were averaged to obtain a single intensity value per protein. Because of the semiquantitative nature of this assay and the use of a single biological sample per condition, results are presented as relative signal intensities.

BODIPY staining of LDs

To assess intracellular lipid accumulation, samples were stained with BODIPY 493/503 (Thermo Fisher Scientific, D3922), a neutral lipid-selective fluorescent dye. A 5 mM BODIPY stock solution was prepared in DMSO and diluted 1:2500 in PBS immediately before use. Samples were first rinsed three times with PBS-T for 5 min each, followed by incubation with the BODIPY working solution at 37°C for 30 min at RT. Excess stain was removed via three additional PBS-T washes, after which samples were fixed in 4% PFA for 15 min at RT. Fixed samples were again washed in PBS-T (3 × 10 min), counterstained with DAPI [1:2000 dilution of stock (5 mg/ml)] and TRITC-phalloidin [1:400 dilution of stock (100 μg/ml)] in PBS-T overnight at 4°C. After a final wash step (3 × 10 min PBS-T), samples were first mounted onto coverslips using the ProLong Gold Antifade Mountant (Thermo Fisher Scientific) and then imaged using a confocal laser scanning microscope (Leica SPE).

CARS microscopy of LDs

To visualize intracellular LDs within 3D constructs, CARS microscopy was used, targeting vibrational signatures of CH-stretching modes. Imaging was conducted on an inverted Nikon Ti2-E microscope equipped with a C2 confocal scanning head and a Nikon CFI Plan Apo IR 100× oil immersion objective (numerical aperture = 1.49). A dual-beam input module (Optique Peter) enabled rapid switching between linear fluorescence and nonlinear CARS imaging modalities. CARS excitation was achieved through coherent interaction of two synchronized pulsed laser beams: from a 1031-nm picosecond fiber laser and a tunable optical parametric oscillator (OPO; APE picoEmerald S) operating at 690 to 960 nm. The OPO was tuned to 797 nm to excite symmetric CH_2 stretching vibrations at 2850 cm^{-1}. The excitation powers at the sample plane were 200 mW (OPO) and 150 mW (Stokes beam). Forward-detected CARS signals were collected using a photomultiplier tube (PMT; Hamamatsu R6357) in conjunction with optical filters (Semrock: FF01-750/SP short-pass and FF01-643/20 band-pass filters). To enhance signal specificity, the 1031-nm Stokes beam was amplitude modulated at 20 MHz and demodulated with a lock-in amplifier (Zurich Instruments HF2LI) locked to the modulation frequency, suppressing nonresonant background contributions. *Z*-stacks were acquired with a step size of 5 μm, capturing >10 optical sections per sample. The pixel dwell time was ~10.8 μs.

Raw image data were processed in ImageJ/Fiji. CARS intensity maps at 2850 cm^{-1} were subjected to Gaussian blur ($\sigma = 1.2$) and background subtraction (rolling ball radius: 30 pixels). LDs were segmented via Otsu thresholding with manual refinement, followed by object separation using the Disconnect Particles plug-in. LD areas were quantified using the analyze particles feature. LD areas were quantified using the analyze particles feature and normalized to the number of DAPI + nuclei. At least nine nonoverlapping image stacks were taken of $n = 3$ independent replicates for each hydrogel formulation.

Image analysis: Protein expression

Quantitative analysis of biomarker expression in GBM cells was performed using CellProfiler (version 4.2.8). For analyses such as Fig. 2D, nuclei were first segmented using DAPI staining to define individual cell objects. Fluorescence intensity corresponding to the target protein (e.g., P-selectin) was then measured within each cell using the "MeasureObjectIntensity" module. Per-cell expression levels were calculated by normalizing total fluorescence intensity to the number of DAPI+ nuclei within each field of view.

All analyses were performed on maximum intensity projections of confocal *z*-stacks to account for 3D signal distribution. Multiple randomized fields of view (at least six images per hydrogel) and at least three independent technical replicates were analyzed to ensure statistical robustness.

Statistical analysis

All data presented in this study were obtained from at least three distinct technical replicates prepared on different experimental days (i.e., different cell passages encapsulated within different hydrogel preparation for each replicate). Experimental results were consistent across various biological replicates and material preparations. Data shown in figures represent independent replicates from biologically distinct experiments. For all imaging-based assays, representative images are derived from experiments repeated at least three times to ensure reproducibility. Statistical analyses were performed using GraphPad Prism (version 10). Specific statistical tests used for each dataset are detailed in the respective figure captions. Unless otherwise stated, comparisons between groups were made using unpaired two-tailed *t* tests or one-way analysis of variance (ANOVA) with

Tukey's post hoc tests for multiple comparisons. Significance was defined as follows: not significant (n.s.; $P > 0.05$), $*P < 0.05$, $**P < 0.01$, $***P < 0.001$, and $****P < 0.0001$. Data are presented as means ± SD unless otherwise indicated.

Supplementary Materials

This PDF file includes:

Table S1
Figs. S1 to S8

REFERENCES

1. Q. T. Ostrom, M. Price, C. Neff, G. Cioffi, K. A. Waite, C. Kruchko, J. S. Barnholtz-Sloan, CBTRUS statistical report: Primary brain and other central nervous system tumors diagnosed in the United States in 2015–2019. *Neuro Oncol.* **24**, v1–v95 (2022).
2. M. Davis, Glioblastoma: Overview of disease and treatment. *Clin. J. Oncol. Nurs.* **20**, S2–S8 (2016).
3. A. Bikfalvi, C. A. Da Costa, T. Avril, J.-V. Barnier, L. Bauchet, L. Brisson, P. F. Cartron, H. Castel, E. Chevet, H. Chneiweiss, A. Clavreul, B. Constantin, V. Coronas, T. Daubon, M. Dontenwill, F. Ducray, N. Entz-Werlé, D. Figarella-Branger, I. Fournier, J.-S. Frenel, M. Gabut, T. Galli, J. Gavard, G. Huberfeld, J.-P. Hugnot, A. Idbaih, M.-P. Junier, T. Mathivet, P. Menei, D. Meyronet, C. Mirjolet, F. Morin, J. Mosser, E. C.-J. Moyal, V. Rousseau, M. Salzet, M. Sanson, G. Seano, E. Tabouret, A. Tchoghandjian, L. Turchi, F. M. Vallette, S. Vats, M. Verreault, T. Virolle, Challenges in glioblastoma research: Focus on the tumor microenvironment. *Trends Cancer* **9**, 9–27 (2023).
4. A. Sohrabi, A. E. Y. T. Lefebvre, M. J. Harrison, M. C. Condro, T. M. Sanazzaro, G. Safarians, I. Solomon, S. Bastola, S. Kordbacheh, N. Toh, H. I. Kornblum, M. A. Digman, S. K. Seidlits, Microenvironmental stiffness induces metabolic reprogramming in glioblastoma. *Cell Rep.* **42**, 113175 (2023).
5. B. Ananthanarayanan, Y. Kim, S. Kumar, Elucidating the mechanobiology of malignant brain tumors using a brain matrix-mimetic hyaluronic acid hydrogel platform. *Biomaterials* **32**, 7913–7923 (2011).
6. K.-J. Streitberger, M. Reiss-Zimmermann, F. B. Freimann, S. Bayerl, J. Guo, F. Arlt, J. Wuerfel, J. Braun, K.-T. Hoffmann, I. Sack, High-resolution mechanical imaging of glioblastoma by multifrequency magnetic resonance elastography. *PLOS ONE* **9**, e110588 (2014).
7. O. Chaudhuri, J. Cooper-White, P. A. Janmey, D. J. Mooney, V. B. Shenoy, Effects of extracellular matrix viscoelasticity on cellular behaviour. *Nature* **584**, 535–546 (2020).
8. K.-J. Streitberger, L. Lilaj, F. Schrank, J. Braun, K.-T. Hoffmann, M. Reiss-Zimmermann, J. A. Käs, I. Sack, How tissue fluidity influences brain tumor progression. *Proc. Natl. Acad. Sci. U.S.A.* **117**, 128–134 (2020).
9. O. Chaudhuri, L. Gu, D. Klumpers, M. Darnell, S. A. Bencherif, J. C. Weaver, N. Huebsch, H. Lee, E. Lippens, G. N. Duda, D. J. Mooney, Hydrogels with tunable stress relaxation regulate stem cell fate and activity. *Nat. Mater.* **15**, 326–334 (2016).
10. W. Fan, K. Adebowale, L. Váncza, Y. Li, M. F. Rabbi, K. Kunimoto, D. Chen, G. Mozes, D. K.-C. Chiu, Y. Li, J. Tao, Y. Wei, N. Adeniji, R. L. Brunsing, R. Dhanasekaran, A. Singhi, D. Geller, S. H. Lo, L. Hodgson, E. G. Engleman, G. W. Charville, V. Charu, S. P. Monga, T. Kim, R. G. Wells, O. Chaudhuri, N. J. Török, Matrix viscoelasticity promotes liver cancer progression in the pre-cirrhotic liver. *Nature* **626**, 635–642 (2024).
11. K. J. Wolf, J. Chen, J. D. Coombes, M. K. Aghi, S. Kumar, Dissecting and rebuilding the glioblastoma microenvironment with engineered materials. *Nat. Rev. Mater.* **4**, 651–668 (2019).
12. A. Elosegui-Artola, A. Gupta, A. J. Najibi, B. R. Seo, R. Garry, C. M. Tringides, I. De Lázaro, M. Darnell, W. Gu, Q. Zhou, D. A. Weitz, L. Mahadevan, D. J. Mooney, Matrix viscoelasticity controls spatiotemporal tissue organization. *Nat. Mater.* **22**, 117–127 (2023).
13. E. M. Carvalho, E. A. Ding, A. Saha, D. C. Garcia, A. Weldy, P. H. Zushin, A. Stahl, M. K. Aghi, S. Kumar, Viscoelastic high-molecular-weight hyaluronic acid hydrogels support rapid glioblastoma cell invasion with leader–follower dynamics. *Adv. Mater.* **36**, e2404885 (2024).
14. S. Sinha, M. Fleck, M. Ayushman, X. Tong, G. Mikos, S. Jones, L. Soto, F. Yang, Matrix stiffness regulates gbm migration and chemoradiotherapy responses via chromatin condensation in 3D viscoelastic matrices. *ACS Appl. Mater. Interfaces* **17**, 10342–10359 (2025).
15. S. Sinha, M. Ayushman, X. Tong, F. Yang, Dynamically crosslinked Poly(ethylene-glycol) hydrogels reveal a critical role of viscoelasticity in modulating glioblastoma fates and drug responses in 3D. *Adv. Healthc. Mater.* **12**, e2202147 (2023).
16. R. Mahesparan, T.-A. Read, M. Lund-Johansen, K. Skaftnesmo, R. Bjerkvig, O. Engebraaten, Expression of extracellular matrix components in a highly infiltrative in vivo glioma model. *Acta Neuropathol.* **105**, 49–57 (2003).
17. C. L. Gladson, The extracellular matrix of gliomas: Modulation of cell function. *J. Neuropathol. Exp. Neurol.* **58**, 1029–1040 (1999).
18. A. C. Bellail, S. B. Hunter, D. J. Brat, C. Tan, E. G. Van Meir, Microregional extracellular matrix heterogeneity in brain modulates glioma cell invasion. *Int. J. Biochem. Cell Biol.* **36**, 1046–1069 (2004).
19. Y. A. Miroshnikova, J. K. Mouw, J. M. Barnes, M. W. Pickup, J. N. Lakins, Y. Kim, K. Lobo, A. I. Persson, G. F. Reis, T. R. McKnight, E. C. Holland, J. J. Phillips, V. M. Weaver, Tissue mechanics promote IDH1-dependent HIF1α–tenascin C feedback to regulate glioblastoma aggression. *Nat. Cell Biol.* **18**, 1336–1345 (2016).
20. I. Angel, O. Pilo Kerman, L. Rousso-Noori, D. Friedmann-Morvinski, Tenascin C promotes cancer cell plasticity in mesenchymal glioblastoma. *Oncogene* **39**, 6990–7004 (2020).
21. R. A. Suhar, M. S. Huang, R. S. Navarro, G. Aviles Rodriguez, S. C. Heilshorn, A library of elastin-like proteins with tunable matrix ligands for *in vitro* 3D neural cell culture. *Biomacromolecules* **24**, 5926–5939 (2023).
22. S. Ferber, G. Tiram, A. Sousa-Herves, A. Eldar-Boock, A. Krivitsky, A. Scomparin, E. Yeini, P. Ofek, D. Ben-Shushan, L. I. Vossen, K. Licha, R. Grossman, Z. Ram, J. Henkin, E. Ruppin, N. Auslander, R. Haag, M. Calderón, R. Satchi-Fainaro, Co-targeting the tumor endothelium and P-selectin-expressing glioblastoma cells leads to a remarkable therapeutic outcome. *Elife* **6**, e25281 (2017).
23. E. Yeini, P. Ofek, S. Pozzi, N. Albeck, D. Ben-Shushan, G. Tiram, S. Golan, R. Kleiner, R. Sheinin, S. Israeli Dangoor, S. Reich-Zeliger, R. Grossman, Z. Ram, H. Brem, T. M. Hyde, P. Magod, D. Friedmann-Morvinski, A. Madi, R. Satchi-Fainaro, P-selectin axis plays a key role in microglia immunophenotype and glioblastoma progression. *Nat. Commun.* **12**, 1912 (2021).
24. M. S. Huang, B. L. LeSavage, S. Ghorbani, A. E. Gilchrist, J. G. Roth, C. Huerta-López, E. A. Mozipo, R. S. Navarro, S. C. Heilshorn, Viscoelastic N-cadherin-like interactions maintain neural progenitor cell stemness within 3D matrices. *Nat. Commun.* **16**, 5213 (2025).
25. Y. Liu, A. E. Gilchrist, P. K. Johansson, Y. Guan, J. D. Deras, Y. Liu, S. Ceva, M. S. Huang, R. S. Navarro, A. Enejder, G. Peltz, S. C. Heilshorn, Engineered hydrogels for organoid models of human nonalcoholic fatty liver disease. *Adv. Sci.* **12**, e17332 (2025).
26. K. K. Veeravalli, S. Ponnala, C. Chetty, A. J. Tsung, M. Gujrati, J. S. Rao, Integrin α9β1-mediated cell migration in glioblastoma via SSAT and Kir4.2 potassium channel pathway. *Cell. Signal.* **24**, 272–281 (2012).
27. M. C. Brown, I. Staniszewska, P. Lazarovici, G. P. Tuszynski, L. Del Valle, C. Marcinkiewicz, Regulatory effect of nerve growth factor in α9β1 integrin–dependent progression of glioblastoma. *Neuro Oncol.* **10**, 968–980 (2008).
28. Y. Yokosaki, N. Matsuura, S. Higashiyama, I. Murakami, M. Obara, M. Yamakido, N. Shigeto, J. Chen, D. Sheppard, Identification of the ligand binding site for the integrin α9β1 in the third fibronectin type III repeat of tenascin-C. *J. Biol. Chem.* **273**, 11423–11428 (1998).
29. H. Schneider, R. P. Harbottle, Y. Yokosaki, J. Kunde, D. Sheppard, C. Coutelle, A novel peptide, PLAEIDGIELTY, for the targeting of $\alpha_9\,\beta_1$ -integrins. *FEBS Lett.* **429**, 269–273 (1998).
30. S. Behrem, K. Zarković, N. Eškinja, N. Jonjić, Distribution pattern of tenascin-C in glioblastoma: Correlation with angiogenesis and tumor cell proliferation. *Pathol. Oncol. Res.* **11**, 229–235 (2005).
31. B. Carnemolla, P. Castellani, M. Ponassi, L. Borsi, S. Urbini, G. Nicolo, A. Dorcaratto, G. Viale, G. Winter, D. Neri, L. Zardi, Identification of a glioblastoma-associated tenascin-C isoform by a high affinity recombinant antibody. *Am. J. Pathol.* **154**, 1345–1352 (1999).
32. F. Yalcin, O. Dzaye, S. Xia, "Tenascin-C function in glioma: Immunomodulation and beyond" in *Tumor Microenvironment*, A. Birbrair, Ed., vol. 1272 of Advances in Experimental Medicine and Biology (Springer International Publishing, 2020), pp. 149–172.
33. B. J. Mahaffey, Z. P. Fowler, Z. Lung, V. Dang, H. Lee, A. M. Johnson, M. A. Munoz, D. A. Goodin, H. B. Frieboes, B. J. Williams, J. Chen, The prognostic effect of mechanical, ultrastructural, and ECM signatures in glioblastoma core and rim. *APL Bioeng.* **8**, 036101 (2024).
34. S. Budday, T. C. Ovaert, G. A. Holzapfel, P. Steinmann, E. Kuhl, Fifty shades of brain: A review on the mechanical testing and modeling of brain tissue. *Arch. Comput. Methods Eng.* **27**, 1187–1230 (2020).
35. S. Budday, G. Sommer, J. Haybaeck, P. Steinmann, G. A. Holzapfel, E. Kuhl, Rheological characterization of human brain tissue. *Acta Biomater.* **60**, 315–329 (2017).
36. S. Budday, G. Sommer, G. A. Holzapfel, P. Steinmann, E. Kuhl, Viscoelastic parameter identification of human brain tissue. *J. Mech. Behav. Biomed. Mater.* **74**, 463–476 (2017).
37. B. L. LeSavage, D. Zhang, C. Huerta-López, A. E. Gilchrist, B. A. Krajina, K. Karlsson, A. R. Smith, K. Karagyozova, K. C. Klett, M. S. Huang, C. Long, G. Kaber, C. M. Madl, P. L. Bollyky, C. Curtis, C. J. Kuo, S. C. Heilshorn, Engineered matrices reveal stiffness-mediated chemoresistance in patient-derived pancreatic cancer organoids. *Nat. Mater.* **23**, 1138–1149 (2024).
38. M. Shayan, M. S. Huang, R. Navarro, G. Chiang, C. Hu, B. P. Oropeza, P. K. Johansson, R. A. Suhar, A. A. Foster, B. L. LeSavage, M. Zamani, A. Enejder, J. G. Roth, S. C. Heilshorn, N. F. Huang, Elastin-like protein hydrogels with controllable stress relaxation rate and stiffness modulate endothelial cell function. *J. Biomed. Mater. Res. A* **111**, 896–909 (2023).
39. A. Saraswathibhatla, D. Indana, O. Chaudhuri, Cell–extracellular matrix mechanotransduction in 3D. *Nat. Rev. Mol. Cell Biol.* **24**, 495–516 (2023).

40. L. G. Griffith, M. A. Swartz, Capturing complex 3D tissue physiology in vitro. *Nat. Rev. Mol. Cell Biol.* **7**, 211–224 (2006).
41. B. M. Baker, C. S. Chen, Deconstructing the third dimension—How 3D culture microenvironments alter cellular cues. *J. Cell Sci.* **125**, 3015–3024 (2012).
42. M. Cescon, E. Rampazzo, S. Bresolin, F. Da Ros, L. Manfreda, A. Cani, A. Della Puppa, P. Braghetta, P. Bonaldo, L. Persano, Collagen VI sustains cell stemness and chemotherapy resistance in glioblastoma. *Cell. Mol. Life Sci.* **80**, 233 (2023).
43. X. Zhang, K. Ding, J. Wang, X. Li, P. Zhao, Chemoresistance caused by the microenvironment of glioblastoma and the corresponding solutions. *Biomed. Pharmacother.* **109**, 39–46 (2019).
44. W. S. Carbonell, M. DeLay, A. Jahangiri, C. C. Park, M. K. Aghi, β1 integrin targeting potentiates antiangiogenic therapy and inhibits the growth of bevacizumab-resistant glioblastoma. *Cancer Res.* **73**, 3145–3154 (2013).
45. H. Janouskova, A. Maglott, D. Y. Leger, C. Bossert, F. Noulet, E. Guerin, D. Guenot, S. Pinel, P. Chastagner, F. Plenat, N. Entz-Werle, J. Lehmann-Che, J. Godet, S. Martin, J. Teisinger, M. Dontenwill, Integrin α5β1 plays a critical role in resistance to temozolomide by interfering with the p53 pathway in high-grade glioma. *Cancer Res.* **72**, 3463–3470 (2012).
46. C. Underhill, CD44: The hyaluronan receptor. *J. Cell Sci.* **103**, 293–298 (1992).
47. W. M. Konsavage, G. S. Yochum, Intersection of Hippo/YAP and Wnt/β-catenin signaling pathways. *Acta Biochim. Biophys. Sin.* **45**, 71–79 (2013).
48. L. He, H. Zhou, Z. Zeng, H. Yao, W. Jiang, H. Qu, Wnt/β-catenin signaling cascade: A promising target for glioma therapy. *J. Cell. Physiol.* **234**, 2217–2228 (2019).
49. H. Clevers, R. Nusse, Wnt/β-catenin signaling and disease. *Cell* **149**, 1192–1205 (2012).
50. S. Zekanovic, P. Achaiber Sing, S. Leenstra, M. L. M. Lamfers, Cut the fat: Targeting cholesterol and lipid metabolism in glioblastoma. *Cell Death Dis.* **16**, 717 (2025).
51. S. Shakya, A. D. Gromovsky, J. S. Hale, A. M. Knudsen, B. Prager, L. C. Wallace, L. O. F. Penalva, H. A. Brown, B. W. Kristensen, J. N. Rich, J. D. Lathia, J. M. Brown, C. G. Hubert, Altered lipid metabolism marks glioblastoma stem and non-stem cells in separate tumor niches. *Acta Neuropathol. Commun.* **9**, 101 (2021).
52. Y. Jin, Y. Tan, J. Wu, Z. Ren, Lipid droplets: A cellular organelle vital in cancer cells. *Cell Death Discov.* **9**, 254 (2023).
53. T.-J. Kao, C.-L. Lin, W.-B. Yang, H.-Y. Li, T.-I. Hsu, Dysregulated lipid metabolism in TMZ-resistant glioblastoma: Pathways, proteins, metabolites and therapeutic opportunities. *Lipids Health Dis.* **22**, 114 (2023).
54. B. Taïb, A. M. Aboussalah, M. Moniruzzaman, S. Chen, N. J. Haughey, S. F. Kim, R. S. Ahima, Lipid accumulation and oxidation in glioblastoma multiforme. *Sci. Rep.* **9**, 19593 (2019).
55. T. T. Le, S. Yue, J.-X. Cheng, Shedding new light on lipid biology with coherent anti-Stokes Raman scattering microscopy. *J. Lipid Res.* **51**, 3091–3102 (2010).
56. T. Hellerer, C. Axäng, C. Brackmann, P. Hillertz, M. Pilon, A. Enejder, Monitoring of lipid storage in *Caenorhabditis elegans* using coherent anti-Stokes Raman scattering (CARS) microscopy. *Proc. Natl. Acad. Sci. U.S.A.* **104**, 14658–14663 (2007).
57. R. Bertolio, F. Napoletano, M. Mano, S. Maurer-Stroh, M. Fantuz, A. Zannini, S. Bicciato, G. Sorrentino, G. Del Sal, Sterol regulatory element binding protein 1 couples mechanical cues and lipid metabolism. *Nat. Commun.* **10**, 1326 (2019).
58. S. Vaidyanathan, T. M. Salmi, R. M. Sathiqu, M. J. McConville, A. G. Cox, K. K. Brown, YAP regulates an SGK1/mTORC1/SREBP-dependent lipogenic program to support proliferation and tissue growth. *Dev. Cell* **57**, 719–731.e8 (2022).
59. S. Kumar, V. M. Weaver, Mechanics, malignancy, and metastasis: The force journey of a tumor cell. *Cancer Metastasis Rev.* **28**, 113–127 (2009).
60. J. Bach, O. Deuster, M. Balzer-Geldsetzer, B. Meyer, R. Dodel, M. Bacher, The role of macrophage inhibitory factor in tumorigenesis and central nervous system tumors. *Cancer* **115**, 2031–2040 (2009).
61. M. Bacher, J. Schrader, N. Thompson, K. Kuschela, D. Gemsa, G. Waeber, J. Schlegel, Up-regulation of macrophage migration inhibitory factor gene and protein expression in glial tumor cells during hypoxic and hypoglycemic stress indicates a critical role for angiogenesis in glioblastoma multiforme. *Am. J. Pathol.* **162**, 11–17 (2003).
62. T. Sameshima, K. Nabeshima, B. P. Toole, K. Yokogami, Y. Okada, T. Goya, M. Koono, S. Wakisaka, Glioma cell extracellular matrix metalloproteinase inducer (EMMPRIN) (CD147) stimulates production of membrane-type matrix metalloproteinases and activated gelatinase A in co-cultures with brain-derived fibroblasts. *Cancer Lett.* **157**, 177–184 (2000).
63. K. Mangano, E. Mazzon, M. S. Basile, R. Di Marco, P. Bramanti, S. Mammana, M. C. Petralia, P. Fagone, F. Nicoletti, Pathogenic role for macrophage migration inhibitory factor in glioblastoma and its targeting with specific inhibitors as novel tailored therapeutic approach. *Oncotarget* **9**, 17951–17970 (2018).
64. D. L. Schonberg, T. E. Miller, Q. Wu, W. A. Flavahan, N. K. Das, J. S. Hale, C. G. Hubert, S. C. Mack, A. M. Jarrar, R. T. Karl, A. M. Rosager, A. M. Nixon, P. J. Tesar, P. Hamerlik, B. W. Kristensen, C. Horbinski, J. R. Connor, P. L. Fox, J. D. Lathia, J. N. Rich, Preferential iron trafficking characterizes glioblastoma stem-like cells. *Cancer Cell* **28**, 441–455 (2015).
65. B. Voth, D. T. Nagasawa, P. E. Pelargos, L. K. Chung, N. Ung, Q. Gopen, S. Tenn, D. T. Kamei, I. Yang, Transferrin receptors and glioblastoma multiforme: Current findings and potential for treatment. *J. Clin. Neurosci.* **22**, 1071–1076 (2015).
66. A. Calzolari, L. M. Larocca, S. Deaglio, V. Finisguerra, A. Boe, C. Raggi, L. Ricci-Vitani, F. Pierconti, F. Malavasi, R. De Maria, U. Testa, R. Pallini, Transferrin receptor 2 is frequently and highly expressed in glioblastomas. *Transl. Oncol.* **3**, 123–134 (2010).
67. F. M. Iwamoto, A. Hormigo, Unveiling YKL-40, from serum marker to target therapy in glioblastoma. *Front. Oncol.* **4**, 90 (2014).
68. F. Szulzewsky, N. Schwendinger, D. Güneykaya, P. J. Cimino, D. Hambardzumyan, M. Synowitz, E. C. Holland, H. Kettenmann, Loss of host-derived osteopontin creates a glioblastoma-promoting microenvironment. *Neuro Oncol.* **20**, 355–366 (2018).
69. H. Jayatilaka, P. Tyle, J. J. Chen, M. Kwak, J. Ju, H. J. Kim, J. S. H. Lee, P.-H. Wu, D. M. Gilkes, R. Fan, D. Wirtz, Synergistic IL-6 and IL-8 paracrine signalling pathway infers a strategy to inhibit tumour cell migration. *Nat. Commun.* **8**, 15584 (2017).
70. M. G. McCoy, D. Nyanyo, C. K. Hung, J. P. Goerger, W. R. Zipfel, R. M. Williams, N. Nishimura, C. Fischbach, Endothelial cells promote 3D invasion of GBM by IL-8-dependent induction of cancer stem cell properties. *Sci. Rep.* **9**, 9069 (2019).
71. I. Sharma, A. Singh, F. Siraj, S. Saxena, IL-8/CXCR1/2 signalling promotes tumor cell proliferation, invasion and vascular mimicry in glioblastoma. *J. Biomed. Sci.* **25**, 62 (2018).
72. F. Seker, A. Cingoz, İ. Sur-Erdem, N. Erguder, A. Erkent, F. Uyulur, M. Esai Selvan, Z. H. Gümüş, M. Gönen, H. Bayraktar, H. Wakimoto, T. Bagci-Onder, Identification of SERPINE1 as a regulator of glioblastoma cell dispersal with transcriptome profiling. *Cancers* **11**, 1651 (2019).
73. O. Chaudhuri, L. Gu, M. Darnell, D. Klumpers, S. A. Bencherif, J. C. Weaver, N. Huebsch, D. J. Mooney, Substrate stress relaxation regulates cell spreading. *Nat. Commun.* **6**, 6364 (2015).
74. J. G. Roth, M. S. Huang, R. S. Navarro, J. T. Akram, B. L. LeSavage, S. C. Heilshorn, Tunable hydrogel viscoelasticity modulates human neural maturation. *Sci. Adv.* **9**, eadh8313 (2023).
75. Y. Hu, Y. Jia, S. Wang, Y. Ma, G. Huang, T. Ding, D. Feng, G. M. Genin, Z. Wei, F. Xu, An ECM-mimicking, injectable, viscoelastic hydrogel for treatment of brain lesions. *Adv. Healthc. Mater.* **12**, 2201594 (2023).
76. J. Lou, R. Stowers, S. Nam, Y. Xia, O. Chaudhuri, Stress relaxing hyaluronic acid-collagen hydrogels promote cell spreading, fiber remodeling, and focal adhesion formation in 3D cell culture. *Biomaterials* **154**, 213–222 (2018).
77. O. Chaudhuri, Viscoelastic hydrogels for 3D cell culture. *Biomater. Sci.* **5**, 1480–1490 (2017).
78. S. Zhang, J. Liu, F. Feng, Y. Jia, F. Xu, Z. Wei, M. Zhang, Rational design of viscoelastic hydrogels for periodontal ligament remodeling and repair. *Acta Biomater.* **174**, 69–90 (2024).
79. P. André, P-selectin in haemostasis. *Br. J. Haematol.* **126**, 298–306 (2004).
80. Y. Shamay, M. Elkabets, H. Li, J. Shah, S. Brook, F. Wang, K. Adler, E. Baut, M. Scaltriti, P. V. Jena, E. E. Gardner, J. T. Poirier, C. M. Rudin, J. Baselga, A. Haimovitz-Friedman, D. A. Heller, P-selectin is a nanotherapeutic delivery target in the tumor microenvironment. *Sci. Transl. Med.* **8**, 345ra87 (2016).
81. D. E. Tylawsky, H. Kiguchi, J. Vaynshteyn, J. Gerwin, J. Shah, T. Islam, J. A. Boyer, D. R. Boué, M. Snuderl, M. B. Greenblatt, Y. Shamay, G. P. Raju, D. A. Heller, P-selectin-targeted nanocarriers induce active crossing of the blood–brain barrier via caveolin-1-dependent transcytosis. *Nat. Mater.* **22**, 391–399 (2023).
82. X. Di, X. Gao, L. Peng, J. Ai, X. Jin, S. Qi, H. Li, K. Wang, D. Luo, Cellular mechanotransduction in health and diseases: From molecular mechanism to therapeutic targets. *Signal Transduct. Target. Ther.* **8**, 282 (2023).
83. S. Dupont, L. Morsut, M. Aragona, E. Enzo, S. Giulitti, M. Cordenonsi, F. Zanconato, J. Le Digabel, M. Forcato, S. Bicciato, N. Elvassore, S. Piccolo, Role of YAP/TAZ in mechanotransduction. *Nature* **474**, 179–183 (2011).
84. Z. Fu, G. Zhu, C. Luo, Z. Chen, Z. Dou, Y. Chen, C. Zhong, S. Su, F. Liu, Matricellular protein tenascin C: Implications in glioma progression, gliomagenesis, and treatment. *Front. Oncol.* **12**, 971462 (2022).
85. S. Marino, G. Menna, R. Di Bonaventura, L. Lisi, P. Mattogno, F. Figà, L. Bilgin, Q. G. D'Alessandris, A. Olivi, G. M. Della Pepa, The extracellular matrix in glioblastomas: A glance at its structural modifications in shaping the tumoral microenvironment—A systematic review. *Cancers* **15**, 1879 (2023).
86. J. Cha, E. A. Ding, E. M. Carvalho, A. Fowler, M. K. Aghi, S. Kumar, Collagen VI deposition primes the glioblastoma microenvironment for invasion through mechanostimulation of β-catenin signaling. *PNAS Nexus* **3**, pgae355 (2024).
87. E. Bae, P. Huang, G. Müller-Greven, D. Hambardzumyan, A. E. Sloan, A. S. Nowacki, N. Marko, C. R. Carlin, C. L. Gladson, Integrin α3β1 promotes vessel formation of glioblastoma-associated endothelial cells through calcium-mediated macropinocytosis and lysosomal exocytosis. *Nat. Commun.* **13**, 4268 (2022).
88. M. Nakada, E. Nambu, N. Furuyama, Y. Yoshida, T. Takino, Y. Hayashi, H. Sato, Y. Sai, T. Tsuji, K. Miyamoto, A. Hirao, J. Hamada, Integrin α3 is overexpressed in glioma stem-like cells and promotes invasion. *Br. J. Cancer* **108**, 2516–2524 (2013).
89. A.-F. Blandin, G. Renner, M. Lehmann, I. Lelong-Rebel, S. Martin, M. Dontenwill, β1 integrins as therapeutic targets to disrupt hallmarks of cancer. *Front. Pharmacol.* **6**, 279 (2015).

90. L. Malric, S. Monferran, J. Gilhodes, S. Boyrie, P. Dahan, N. Skuli, J. Sesen, T. Filleron, A. Kowalski-Chauvel, E. Cohen-Jonathan Moyal, C. Toulas, A. Lemarié, Interest of integrins targeting in glioblastoma according to tumor heterogeneity and cancer stem cell paradigm: An update. *Oncotarget* **8**, 86947–86968 (2017).
91. X. Chen, X. Zhong, F. Zhang, X. Zhou, X. Yue, X. Li, Molecular mechanisms and therapeutic targets in glioblastoma multiforme: Network and single-cell analyses. *Sci. Rep.* **15**, 10558 (2025).
92. G. Safarians, A. Sohrabi, I. Solomon, W. Xiao, S. Bastola, B. W. Rajput, M. Epperson, I. Rosenzweig, K. Tamura, B. Singer, J. Huang, M. J. Harrison, T. Sanazzaro, M. C. Condro, H. I. Kornblum, S. K. Seidlits, Glioblastoma spheroid invasion through soft, brain-like matrices depends on hyaluronic acid–CD44 interactions. *Adv. Healthc. Mater.* **12**, e2203143 (2023).
93. B. A. Krajina, B. L. LeSavage, J. G. Roth, A. W. Zhu, P. C. Cai, A. J. Spakowitz, S. C. Heilshorn, Microrheology reveals simultaneous cell-mediated matrix stiffening and fluidization that underlie breast cancer invasion. *Sci. Adv.* **7**, eabe1969 (2021).
94. J. R. Staunton, W. Y. So, C. D. Paul, K. Tanner, High-frequency microrheology in 3D reveals mismatch between cytoskeletal and extracellular matrix mechanics. *Proc. Natl. Acad. Sci. U.S.A.* **116**, 14448–14455 (2019).
95. S. G. Pfisterer, G. Gateva, P. Horvath, J. Pirhonen, V. T. Salo, L. Karhinen, M. Varjosalo, S. J. Ryhänen, P. Lappalainen, E. Ikonen, Role for formin-like 1-dependent acto-myosin assembly in lipid droplet dynamics and lipid storage. *Nat. Commun.* **8**, 14858 (2017).
96. C. Ibar, K. D. Irvine, Integration of hippo-YAP signaling with metabolism. *Dev. Cell* **54**, 256–267 (2020).
97. J. Cai, T. Chen, Z. Jiang, J. Yan, Z. Ye, Y. Ruan, L. Tao, Z. Shen, X. Liang, Y. Wang, J. Xu, X. Cai, Bulk and single-cell transcriptome profiling reveal extracellular matrix mechanical regulation of lipid metabolism reprograming through YAP/TEAD4/ACADL axis in hepatocellular carcinoma. *Int. J. Biol. Sci.* **19**, 2114–2131 (2023).
98. J. L. Gregory, M. T. Leech, J. R. David, Y. H. Yang, A. Dacumos, M. J. Hickey, Reduced leukocyte–endothelial cell interactions in the inflamed microcirculation of macrophage migration inhibitory factor–deficient mice. *Arthritis Rheum.* **50**, 3023–3034 (2004).
99. R. Schmidt, A. Bültmann, S. Fischel, A. Gillitzer, P. Cullen, A. Walch, P. Jost, M. Ungerer, N. D. Tolley, S. Lindemann, M. Gawaz, A. Schömig, A. E. May, Extracellular matrix metalloproteinase inducer (CD147) Is a novel receptor on platelets, activates platelets, and augments nuclear factor κB–dependent inflammation in monocytes. *Circ. Res.* **102**, 302–309 (2008).
100. C. A. Formolo, R. Williams, H. Gordish-Dressman, T. J. MacDonald, N. H. Lee, Y. Hathout, Secretome signature of invasive glioblastoma multiforme. *J. Proteome Res.* **10**, 3149–3159 (2011).
101. B. L. LeSavage, N. A. Suhar, C. M. Madl, S. C. Heilshorn, Production of elastin-like protein hydrogels for encapsulation and immunostaining of cells in 3D. *J. Vis. Exp.* **135**, 57739 (2018).
102. M. E. Hefferon, M. S. Huang, Y. Liu, R. S. Navarro, N. De Paiva Narciso, D. Zhang, G. Aviles-Rodriguez, S. C. Heilshorn, Cell microencapsulation within engineered hyaluronan elastin-like protein (HELP) hydrogels. *Curr. Protoc.* **3**, e917 (2023).

Acknowledgments

Funding: S.G. acknowledges support from Stanford Bio-X and the Novo Nordisk Foundation (NNF22OC0073507). M.S.H. acknowledges support from the Sarafan ChEM-H Chemistry/Biology Interface Program as an O'Leary-Thiry Fellow, a National Science Foundation (NSF) Graduate Research Fellowship (DGE-1656518), a National Institutes of Health (NIH) NRSA Pre-doctoral Fellowship (F31-NS132505), and the Gerald J. Lieberman Fellowship. D.Z. acknowledges support from the National Science Foundation (NSF) Graduate Research Fellowship (DGE-1656518) and the Stanford Graduate Fellowship. R.R.R. acknowledges support from the NIH on the NIH K12- HD000850 from the Eunice Kennedy Shriver National Institute of Child Health and Human Development (NICHD), the Stanford Maternal and Child Health Research Institute Clinical Trainee Award, the Stanford Department of Pediatrics Physician–Scientist Bridge to K Support. S.C.H. acknowledges support from the Stanford Cancer Institute Seed Grant and NIH (R61 CA278450 and R01 MH137333) and NSF (DMR 2427971). **Author contributions:** Conceptualization: S.G., M.S.H., and S.C.H. Data curation: S.G. and S.C.H. Formal analysis: S.G., M.S.H., D.Z., C.L., Y.L., and E.A.T.M. Funding acquisition: S.G. and S.C.H. Investigation: S.G., M.S.H., D.Z., C.L., R.Z., Y.L., R.R.R., and E.A.T.M. Methodology: S.G., M.S.H., S.C.H., C.L., and R.R.R. Project administration: S.G. and S.C.H. Resources: S.G., M.S.H., S.C.H., C.L., and A.E. Software: S.G. and E.M. Supervision: S.G., A.E., and S.C.H. Validation: S.G., M.S.H., S.C.H., D.Z., and Y.L. Visualization: S.G., S.C.H., D.Z., and Y.L. Writing—original draft: S.G. and E.A.T.M. Writing—review and editing: S.G., M.S.H., S.C.H., D.Z., C.L., Y.L., R.R.R., A.E., and E.A.T.M. **Competing interests:** S.C.H. is an inventor on a patent application related to this work filed by Stanford University. The authors declare that they have no other competing interests. **Data, code, and materials availability:** All data and code needed to evaluate and reproduce the results in the paper are present in the paper and/or the Supplementary Materials. This study did not generate new materials.

Submitted 21 January 2026
Accepted 10 July 2026
Published 21 August 2026
10.1126/sciadv.aef7087

ScienceAdvances

Matrix stress relaxation drives glioblastoma cell response in viscoelastic biomaterials

Sadegh Ghorbani, Michelle S. Huang, Daiyao Zhang, Yueming Liu, Christopher Long, Riley Zwetsloot, Esther A.T. Mozipo, Rameshwar R. Rao, Annika Enejder, and Sarah C. Heilshorn

Sci. Adv. **12** (34), eaef7087. DOI: 10.1126/sciadv.aef7087

Science Advances (ISSN 2375-2548) is published by the American Association for the Advancement of Science. 1200 New York Avenue NW, Washington, DC 20005. The title *Science Advances* is a registered trademark of AAAS.